Volume 1
Number 5
September 2023
Pages 583–786

EES Catalysis

rsc.li/EESCatalysis

ISSN 2753-801X

ROYAL SOCIETY OF CHEMISTRY

REVIEW ARTICLE
Sangaraju Shanmugam *et al.*
Recent advances in electrocatalytic NO_x reduction into ammonia

EES Catalysis

REVIEW ARTICLE

View Article Online
View Journal | View Issue

Cite this: *EES Catal.*, 2023, 1, 645

Recent advances in electrocatalytic NO_x reduction into ammonia

Harish Reddy Inta, Dinesh Dhanabal, Sridhar Sethuram Markandaraj and Sangaraju Shanmugam *

Ammonia (NH_3) is an essential ingredient for the production of numerous chemicals which have a wider usage as fertilizers, explosives, and plastics. Currently, NH_3 is mainly produced from the conventional Haber–Bosch process, which is energy-consuming and involves the risk of emitting greenhouse gases into the atmosphere. In contrast, electrochemical ammonia synthesis (EAS) from the nitrogen reduction reaction is evolving as a viable solution for sustainable NH_3 production under ambient conditions. However, the high N≡N dissociation energy and the competitive hydrogen evolution reaction result in an unsatisfactory ammonia yield rate and Faradaic efficiency. In this regard, EAS from reactive nitrogen (NO_x) species, especially through the nitric oxide reduction reaction (NORR), could be a sustainable way as it produces valuable NH_3 and simultaneously mitigates the gaseous NO_x pollutant. Various NORR electrocatalysts have been designed and investigated. The electrocatalytic activity hugely depends on the composition, Gibbs free energy for 'NO' or intermediate adsorption on the catalyst surface, and the rate of proton/electron transfer at the solid–liquid–gas interface. Besides, different electrolyte additives have been employed to improve the solubility of NO in aqueous electrolytes. Thus, this review presents an overview of the NORR mechanism, recent advancements in electrocatalysts, and factors influencing the NH_3 yield and selectivity. After that, the forthcoming challenges associated with practical realisation of EAS *via* NORR are discussed.

Received 24th April 2023,
Accepted 1st June 2023

DOI: 10.1039/d3ey00090g

rsc.li/eescatalysis

Broader context

Recently, electrochemical ammonia synthesis (EAS) has drawn significant attention for replacing the energy consuming and environmentally polluting Haber–Bosch process. In this context, the electrochemical nitrogen reduction reaction (NRR) is considered to be a viable solution for sustainable NH_3 production under ambient conditions. However, the high N≡N dissociation energy and the competitive hydrogen evolution reaction cause challenges to attain satisfactory ammonia production with good selectivity. Meanwhile, the nitric oxide (NO_x) pollutant could be an alternative N-source for EAS as it possesses low N=O bond dissociation energy and a distinctive reduction potential (0.71 V *vs.* RHE). To catalyze the electrochemical nitric oxide reduction reaction (NORR), the development of suitable catalysts with good catalytic activity and product (NH_3) selectivity is highly desirable. Hence, the scientific community has attempted to design and develop various electrocatalysts and evaluate their performance towards the NORR. The electrocatalytic activity of the materials is found to be dependent on the composition, Gibbs free energy for 'NO' or intermediate adsorption on the catalyst surface, and the rate of proton/electron transfer at the solid–liquid–gas interface. Besides, the addition of 'NO' complexing agents into an aqueous electrolyte is found to increase the solubility of 'NO', thereby enhancing the ammonia production rate. Although the developed catalysts show considerable NH_3 yield rates, there is still a necessity to develop efficient and earth-abundant catalysts for practical NH_3 production. Hence, we present this Review article to give an overview of the NORR mechanism, recent advancements in the electrocatalysts, and factors influencing the NH_3 yield and selectivity. Furthermore, the key issues related to the efficient electroreduction of NO to NH_3 are described.

Introduction

The thirst for energy keeps expanding with the growing technological society of humankind in this modern era.[1] The rise in the human population, urbanization, and industrial activities increases the energy demand worldwide.[2–6] This huge energy demand results in the over-exploitation of fossil fuels and causes a surge in carbon and greenhouse gas (GHG) emissions. These emissions trap the thermal radiation in the earth's atmosphere, raise the global temperature, and cause climate change.[7] Thus, the energy crisis leads to domino effects related to global warming and accelerated climate change.[8]

Department of Energy Science & Engineering, Daegu Gyeongbuk Institute of Science & Technology (DGIST), Daegu 42988, Republic of Korea.
E-mail: sangarajus@dgist.ac.kr

With reference to the U.S. Energy Information Administration (EIA) data in 2021, the transportation sector utilizes around 28% of the total energy consumption of the U.S., which is mainly derived from fossil fuels.[9] In the transportation sector, maritime transport controls 90% of global goods trading, accounting for 3.1% of global CO_2 emissions.[10,11] To mitigate environmental pollution, the Intergovernmental Panel on Climate Change (IPCC) formed a crucial strategy of decarbonizing the transport sector to reach the goals of the Paris climate change agreement to limit global temperature raise within 1.5 °C of pre-industrial levels.[12,13] Therefore, the International Maritime Organization (IMO) set several checkpoints to complete the decarbonization of maritime transportation. The IMO GHG strategy sets out to reduce CO_2 emission per transport work by up to 40% by 2030 and 70% by 2050 as of 2008 emission levels.[14,15] Utilizing zero-carbon fuels in marine transport is the key strategy of IMO to meet the aims of the GHG strategy. Ammonia has attracted everyone's attention as a potential zero-carbon fuel for maritime transport and has been applied in direct ammonia fuel cells and solid oxide fuel cells (SOFCs).[16,17] Compared with liquid hydrogen (8.5 MJ L^{-1}), ammonia possesses a high energy density of 12.7 MJ L^{-1}.[18] Moreover, storing ammonia at −33 °C with less energy consumption for storage is more convenient, whereas hydrogen needs a cryogenic condition of −235 °C.[19,20] With these considerations, many researchers foresee ammonia as a potential decarbonization fuel for heavy transportation like maritime transport.[21–24]

Besides, ammonia (NH_3) is a crucial substance for various industries to produce fertilizers, medicines, refrigerants, explosives, and pesticides. Thus, NH_3 is extensively produced from a

Harish Reddy Inta

Harish Reddy Inta received his PhD degree in Chemical Sciences from Indian Institute of Science Education and Research-Kolkata (IISER-K), India in 2022. He is currently working as a postdoctoral researcher at Daegu Gyeongbuk Institute of Science & Technology (DGIST), Daegu, Republic of Korea. His current research interest is on the development of efficient catalysts for electrosynthesis of value-added chemicals such as NH_3 and urea from air pollutants (NO_x and CO_2).

Dinesh Dhanabal

Dinesh Dhanabal received his BTech degree in Chemical and Electrochemical Engineering from CSIR-Central Electrochemical Research Institute (CECRI), Karaikudi, India in 2020. He is currently pursuing his Masters' degree in Energy Science and Engineering at Daegu Gyeongbuk Institute of Science & Technology (DGIST), Dabegu, Republic of Korea, under the supervision of Prof. Sangaraju Shanmugam. His research interest is focussed on development of cost effective and efficient electrocatalysts for the synthesis of value-added chemicals such as NH_3 and urea from air pollutants (NO_x and CO_2).

Sridhar Sethuram Markandaraj

Sridhar Sethuram Markandaraj received his BTech degree in Chemical and Electrochemical Engineering from CSIR-Central Electrochemical Research Institute (CECRI), Karaikudi, India in 2020. Recently, he secured his Masters' degree in Energy Science and Engineering at Daegu Gyeongbuk Institute of Science & Technology (DGIST), Daegu, Republic of Korea, under the supervision of Prof. Sangaraju Shanmugam. His research interests include electrocatalytic nitric oxide reduction to value-added chemicals.

Sangaraju Shanmugam

Sangaraju Shanmugam obtained his doctorate in 2004 from the Indian Institute of Technology-Madras (IIT-M), India in the field of heterogeneous catalysis. Thereafter, in 2005, he joined the Department of Chemistry, Bar-Ilan University, Israel as a Postdoctoral Fellow. In 2007, he joined as a JSPS postdoctoral fellow at Waseda University and continued his research in "Catalysis for energy applications". In 2011, he continued his academic career as an Assistant Professor at Daegu Gyeongbuk Institute of Science & Technology (DGIST), Republic of Korea and was promoted to Tenured Full Professor in 2019. His research interests include cost-effective membranes and catalysts for fuel cell and redox-flow batteries and electrosynthesis of value-added chemicals from atmospheric nitrogen and air pollutants.

well-established very old Haber–Bosch Process (HBP).[25] However, the ammonia produced by the conventional HBP is not a green commodity. The required hydrogen feedstock for the HBP is exclusively extracted from fossil fuels by steam methane reforming or coal gasification processes. Thus, the HBP consumes 2% of global fossil fuel usage. As the HBP depends on the fossil fuel for the H_2 source, it is not a sustainable and greener process. The ammonia production by the energy consuming HBP currently accounts for 2% of global energy consumption and 1.4% of global CO_2 emission (carbon emission during gas extraction is excluded).[21,26] Therefore, the decarbonization of ammonia production will decarbonize the energy, transportation, and chemical sectors so that the effects of GHG emissions and climate change can be controlled. MacFarlane *et al.* pointed out that the ammonia industry's decarbonization will occur in three phases, with different technologies.[21] As shown in Fig. 1, today the "grey ammonia" is exclusively produced from fossil fuels with the enormous release of CO_2 into the environment. Therefore, the first generation will utilize carbon capture and storage technology to capture all the CO_2 emissions from HBP (and SMR) to produce "purple ammonia". The second generation will produce "blue ammonia" or "renewable ammonia". At this stage, the HBP will be electrified with renewable energy and the hydrogen feedstock will be switched from fossil resources to green hydrogen produced by water electrolysis. Eventually, in the third generation, the HBP will no longer be needed as the renewable energy-assisted electrochemical reduction of the N-source and the H-source from water will be commercialized to produce "sustainable ammonia" or "green-ammonia".

The energy-intensive HBP is carried out under harsh conditions such as high temperature (300–500 °C) and high pressure (150–200 atm). Moreover, each pass in the HBP results in only 15% conversion efficiency and it needs multiple passes to achieve a high conversion efficiency of 97%.[27] Therefore, it is a substantial challenge to develop alternative routes to produce NH_3 in a sustainable way. Recently, electrochemical NH_3 synthesis (EAS) through the nitrogen reduction reaction (NRR) has greatly attracted attention for the production of NH_3 under ambient conditions.[28,29] The electroreduction of N_2 to NH_3 only requires protons (H^+) from water and the electricity drawn from renewable energy resources, and could be conducted under ambient conditions with no carbon emission.[30–34] However, the electrochemical ammonia yield from the NRR is unsatisfactory

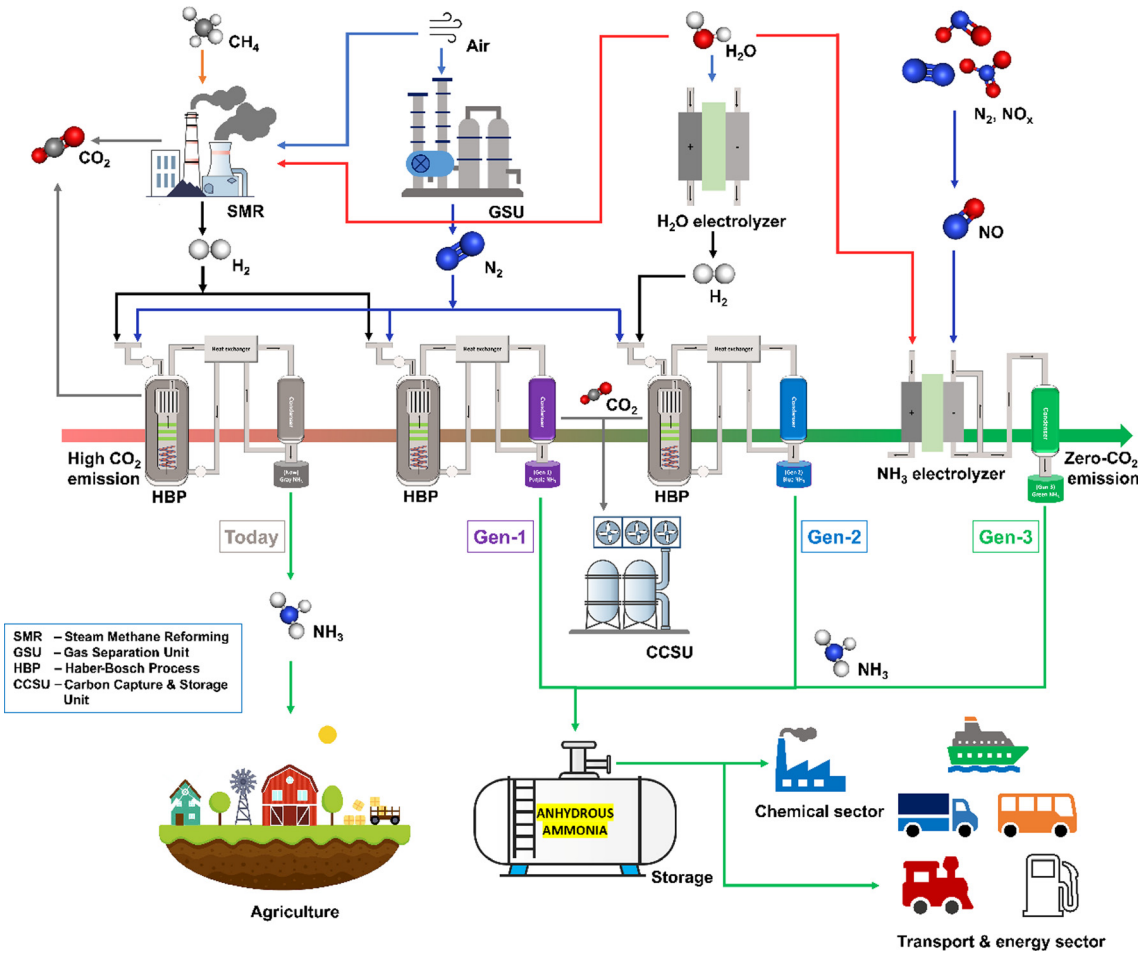

Fig. 1 Ammonia economy roadmap showing current and projected contributions of the current and Gen 1 (purple), Gen 2 (light blue), and Gen 3 (green) ammonia production technologies.

because of high N≡N bond dissociation energy, low polarizability, and limited solubility of electrolytes. In addition, the competitive hydrogen evolution reaction (HER) in the NRR potential range (0.148 V *vs.* RHE) is another bottleneck to attaining high NH_3 Faradaic efficiency.[30,35] In contrast to N_2, nitric oxide (NO) is partly active due to its lower bond energy (N=O 607 kJ mol^{-1}, N≡N 941 kJ mol^{-1} at 25 °C).[36] The electronic structure of NO containing unpaired electrons and the lower energy of its $2\pi^*$ orbital make it noticeably polar and reactive to undergo electrochemical reactions.[37] NO possesses a positive electron affinity (0.024 eV) and a lower ionization potential (9.2 eV) compared to molecular N_2 (−1.9 eV and 15.8 eV, respectively), allowing it to be more readily active toward redox reactions.[38,39] Moreover, the standard reduction potential for NO to NH_3 is about 0.71 V *vs.* RHE, which is advantageous to attain a high NH_3 yield along with high Faradaic efficiency.[40,41]

Besides, groundwater pollutants (such as NO_3^- and NO_2^-) have also been used as reactive nitrogen species for EAS. Meanwhile, this process could be a promising alternative to biological denitrification and physical separation processes for removing nitrate ions from wastewater.[42] Despite the electroreduction of nitrogen species that could lead to the formation of various products such as N_2, N_2O, NH_3, and NH_2OH, the thermodynamic potentials for NH_3 production are as follows:[41,43]

$$NO_3^- + 9H^+ + 8e^- \rightarrow NH_3 + 3H_2O \quad E_0 = 0.88 \text{ V } \textit{vs.} \text{ RHE} \tag{1}$$

$$NO_2^- + 7H^+ + 6e^- \rightarrow NH_3 + 2H_2O \quad E_0 = 0.86 \text{ V } \textit{vs.} \text{ RHE} \tag{2}$$

$$NO + 5H^+ + 5e^- \rightarrow NH_3 + H_2O \quad E_0 = 0.71 \text{ V } \textit{vs.} \text{ RHE} \tag{3}$$

The EAS by the electroreduction of NO_3^- and NO_2^- is a more energy consuming and complex process compared with the NRR and NO reduction reaction (NORR) owing to the involvement of more number of electrons in the former (*i.e.*, NO_3^- and NO_2^- electroreduction requires 8 and 6 electrons, whereas the NORR requires only 5 electrons).[44–49] In addition, NO_3^-/NO_2^- to NH_3 production proceeds through the formation of 'NO' as a key intermediate.[50,51] Besides, NO_3^- and NO_2^- electroreductions are liquid phase reactions, so it would require additional expenses and systems to separate the electrochemically synthesized NH_3 from the electrolyte. In contrast, EAS through the NORR is advantageous for practical implementation as the NORR can be conducted in the gas phase using a membrane electrode assembly, and the present gas separation and liquefying units in HBP plants can be reused.

On the other hand, mitigating hazardous NO_x species from the atmosphere is a substantial challenge as it reacts with atmospheric oxygen and moisture to produce nitrous or nitric acid, which causes acid rain, smog, *etc.*[52] The current technology used to convert hazardous NO_x into harmless N_2 is selective catalytic reduction (SCR), which uses valuable NH_3 and H_2 as reductants.[53,54] The SCR also requires high temperature and pressure application to reduce NO_x to N_2, which has no chemical use. Thus, the development of efficient technologies to remove NO_x from the atmosphere is a substantial challenge. In this regard, the NORR into NH_3, N_2, *etc.*, through renewable energy resources such as solar and wind, could be a viable and practical solution. Thus, electrochemical NORR to NH_3 production is a kind of "kill two birds with one stone" strategy as it mitigates the NO_x pollutant and produces a value-added product. Additionally, as a potential alternative to the traditional HBP, NORR electrolysis will decarbonize the above-mentioned energy, transport, and chemical industries to save the global ecology. However, the practical implementation of this technology is hugely dependent on the development of efficient electrocatalysts that can catalyze the NORR at low overpotentials along with good product selectivity. Hence, this review provides an overview of the NORR mechanism, recent advancements in electrocatalyst development, and factors influencing the NH_3 yield and selectivity. In addition, the associated challenges that still need to be addressed for the practical realization of EAS as an alternative to the HBP will be discussed.

Mechanism of NO_x reduction

The electrocatalytic NORR process can produce various products such as hydroxylamine (NH_2OH), ammonia (NH_3), nitrous oxide (N_2O), and nitrogen (N_2) owing to the multi-electron coupled proton reactions. The thermodynamic potentials for the corresponding products are as follows:

$$NO + 3\left(H^+ + e^-\right) \rightarrow NH_2OH \quad E_0 = 0.38 \text{ V } \textit{vs.} \text{ RHE} \tag{4}$$

$$NO + 5\left(H^+ + e^-\right) \rightarrow NH_3 + H_2O \quad E_0 = 0.71 \text{ V } \textit{vs.} \text{ RHE} \tag{5}$$

$$2NO + 2\left(H^+ + e^-\right) \rightarrow N_2O + H_2O \quad E_0 = 1.59 \text{ V } \textit{vs.} \text{ RHE} \tag{6}$$

$$2NO + 4\left(H^+ + e^-\right) \rightarrow N_2 + 2H_2O \quad E_0 = 1.68 \text{ V } \textit{vs.} \text{ RHE} \tag{7}$$

In addition, hydrogen (H_2) can be formed at more cathodic potentials (below 0 V *vs.* RHE). The product selectivity of the NORR is hugely dependent on the catalyst surface, applied potential, 'NO' coverage, *etc.* For instance, the NORR over nanostructured Pd/C has only produced H_2, while the PdCu/C catalyst has generated N_2 as a main product (~68%) by forming NH_3 and N_2H_4 as side products.[55] Meanwhile, Cu exhibits higher selectivity towards NH_3.[34] Thus, the chemical composition and the electronic structure of the catalyst are the key to obtaining desirable products. Electrode potential also plays a significant role in product selectivity. Both theoretical and experimental studies on transition metal electrodes manifest that at more positive potentials (>0.3 V) N_2O forms as a main product, whereas NH_3 can be generated along with H_2 at more negative potentials.[56] N_2 and NH_2OH products can be observed at the intermediate potential window. Besides, low 'NO' coverage over the catalyst surface preferentially produces single-N products (NH_3, NH_2OH), while high coverage leads to 'NO' dimerization resulting in the N–N coupled product (N_2, N_2O) formation.[57]

During the NORR, initially 'NO' adsorption on the catalyst surface occurs with different configurations such as N-end, O-

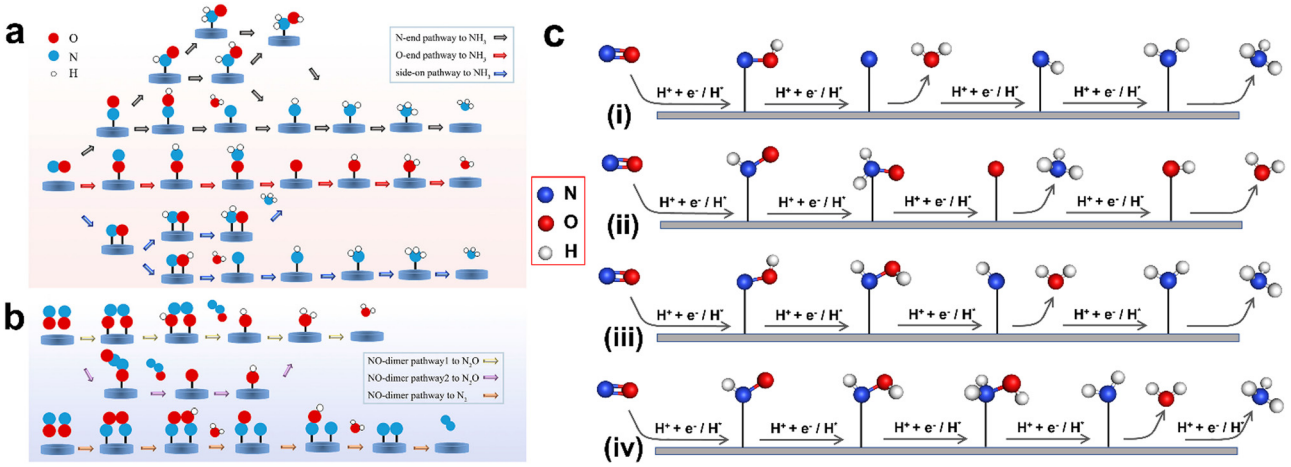

Fig. 2 (a) Schematic pathways of the NORR process toward NH_3 synthesis. (b) Schematic pathways of the NORR process toward N_2O/N_2 synthesis. Reproduced with permission from ref. 67, copyright 2022, ACS. (c) Scheme of distal-O (i), distal-N (ii), alternating-O (iii), and alternating-N pathways (iv), which are all assigned to the associative mechanism. The $H^+ + e^-$ and H* represent protons and adsorbed H*, corresponding to the Heyrovsky and Tafel-type hydrogenation, respectively.

end, and side-on. The subsequent electron transfer leads to the formation of various reaction intermediates and products (Fig. 2). The 'NO' adsorption to NH_3 occurs *via* either a dissociative or associative pathway. In the dissociative pathway, the first step is splitting the N–O bond on the active site. Then, each adsorbed atom (N* or O*) will be hydrogenated separately to yield NH_3 and H_2O. In the case of the associative pathway, both 'N' and 'O' atoms in the NO molecule will be protonated consequently to produce a 'H_xNOH_y' intermediate, which will eventually reduce to NH_3. In both routes, the hydrogenation process proceeds *via* either the Tafel or Heyrovsky-type mechanism. In the former case, prior to the 'NO' hydrogenation, the solvated protons will be adsorbed onto the catalyst's surface to from H*, whereas the hydrogenation of 'NO' molecules or the intermediates occurs directly on the catalyst surface in the latter case. Based on the type of hydrogenation, the dissociative and associative pathways are further divided into four categories, termed as dissociative-Tafel (D-T), associative-Tafel (A-T), dissociative-Heyrovsky (D-H), and associative-Heyrovsky (H-A) mechanisms.[34] Furthermore, the associative mechanisms are classified into distal-O, distal-N, alternating-O, and alternating-N pathways. In the distal pathway, one of the two atoms (N or O) in NO will be completely hydrogenated to produce NH_3 or H_2O. Thereafter, O* or N* will undergo the hydrogenation process. In contrast, both N and O atoms undergo alternative hydrogenation steps in the alternating pathway.

Due to the involvement of multi-electron transfers, there are numerous varieties of mechanisms, intermediates, and rate-determining steps proposed for the NORR in the literature. The mechanistic studies are initially performed on the Pt surface in an aqueous electrolyte using various techniques such as voltammetry, *in situ* infrared spectroscopy, and online mass spectroscopy.[37,58,59] Earlier, Colucci *et al.* suggested that continuous NO reduction occurs through the rate-determining step (RDS) of $NO^* + H^+ + e^- \rightarrow NOH^*$.[60] After that, Gootzen *et al.* demonstrated the involvement of the NO dissociation step ($NO^* \rightarrow N^* + O^*$) in the mechanism.[61] Meanwhile, the adsorbate reduction (NO adsorbed onto the Pt electrode) and continuous reduction (NO saturated electrolyte) products of the NORR are found to be different. Later, Vooys *et al.* clarified the mechanistic pathways in both scenarios with the help of kinetic parameters and product selectivity by utilizing the potential, pH, NO surface coverage, and the effect of supporting electrolytes as variables.[58] During the adsorbate NO reduction in an acidic medium, NH_3 is predominantly formed, whereas the continuous NO reduction yields N_2O and NH_3 products at above and below 0.4 V, respectively. The similar Tafel slope observed for the first two reduction peaks in adsorbate NO reduction indicates that the first proton-coupled electron transfer is in electrochemical equilibrium, and NH_3 will be generated through the N–O bond breaking after the RDS, as given below.

$$NO^* + H^+ + e^- \rightarrow HNO^* \text{ (equilibrium)} \quad (8)$$

$$HNO^* + H^+ + e^- \rightarrow H_2NO^* \text{ (RDS)} \quad (9)$$

$$H_2NO^* + 3H^+ + 3e^- \rightarrow NH_4^+ + H_2O \text{ (fast)} \quad (10)$$

At below 0.4 V, the continuous NO reduction also produces the NH_3 in a similar mechanistic pathway. Above 0.4 V, N_2O is produced through the dimerization of NO* with the 'NO' present in the solution. In another report, Rosca *et al.* proposed that the NORR mechanism on Pt (100) follows the $NO \rightarrow HNO^* \rightarrow NH^* + O^* \rightarrow NH_3 + H_2O$ pathway, in which $HNO^* \rightarrow NH^* + O^*$ is the RDS.[59] Thereafter, several DFT studies were also carried out to attempt to understand the exact mechanism over the Pt surface.[62–64] However, the conclusive mechanism could not be derived as the kinetic barriers were not considered in these studies.[65]

Besides Pt, the NORR mechanism was studied on various transition metals such as Pd, Rh, Ru, Ir, and Au.[66] Except Au, all the metals showed high selectivity towards N_2O and NH_3 at more positive and negative potentials, respectively, like Pt. The similar onset potentials of all metals indicate that the N_2O

formation occurs through a common mechanism, while the various Tafel slopes manifest the different RDSs over metal surfaces. This could be most likely due to the shift in the occurrence of the first electron-transfer step during the catalytic process. Among all the metals, Pd is found to be the most active catalyst for selective N_2 formation *via* the N_2O intermediate. However, the NO to NH_3 mechanism over these metals is still unclear.

Recently, several DFT studies attempted to correlate the NORR activity of various metals by using the adsorption energies of *NO and *N intermediates as descriptors.[43,67,68] Furthermore, to understand the selectivity of NH_3 formation over H_2, the adsorption energy of *H is also considered. As shown in Fig. 3a, metals present on the left of the vertical line (Pt and Pd) show higher binding ability towards both *NO and *H, leading to dominant H_2 production below 0 V_{RHE}. The NH_3 formation over the metals located above the horizontal line (Ag and Au) is limited due to the weak binding of *NO. Meanwhile, Cu shows selective binding towards *NO over *H, thereby indicating ideal catalytic behavior towards NH_3 formation.[43] Furthermore, the limiting potential *vs.* adsorption energy of *N plot shows that Cu is located on the weak binding side. Cu is predicted to follow the distal-O pathway to produce NH_3, and the rate-limiting step is *NO → *NHO (Fig. 3b). The limiting potential of 'Cu' can be reduced by adjusting the metal surface with a slightly negative adsorption energy (not higher than −1.5 eV) of *N. Besides, the DFT studies performed on different metal compounds predicted that the NH_3 formation occurs through various mechanistic pathways, intermediates, and RDSs.[54,69] In transition metal compounds, the significant overlap between the metal d-orbitals and the π orbitals of NO is the primary criterion for the adsorption and activation of NO molecules through the "acceptance–donation" mechanism, *i.e.*, simultaneous depletion and accumulation of electron density in NO orbitals.[54] The above studies indicate that the NORR activity and product selectivity are determined by various parameters such as the catalyst surface, operating potential, NO coverage, and hence, the favorable pathways and RDSs over the catalytic materials could differ.

Electrocatalysts for the NO_x reduction reaction (NORR)

Different classes of materials have been developed to investigate their electrocatalytic performance towards the NORR. Based on the chemical composition, the electrode materials can be classified into three categories: precious transition metal-based, non-precious transition metal-based, and p-block element-based electrocatalysts. Meanwhile, several attempts were made to identify the reaction intermediates and unveil the possible reaction mechanism of the NORR over the catalyst surfaces, which will guide the design and production of efficient electrocatalysts with good product selectivity. This section will briefly describe the materials and their catalytic activity in terms of overpotential, selectivity, NH_3 yield rates, and Faradaic efficiency (FE). In addition, the efforts toward identifying reaction intermediates to understand the NO_x mechanism through computational and experimental studies will be discussed.

1. Precious transition metal-based electrocatalysts

Precious metals such as Pt, Pd, and Ru are renowned for numerous electrocatalytic applications owing to their high electronic conductivity and the ability to bind the various reaction intermediates on their polycrystalline surfaces.[70] Despite these metals being found to be active catalysts towards the NORR, the product selectivity is hugely varied as the catalytic surfaces possess different inherent Gibbs free energies for adsorption of NO* and H* intermediates. In the 20th century, the research was extensively focused on the mechanistic investigation of NORR activity over platinum surfaces. In contrast, the recent focus has shifted towards developing efficient electrocatalysts with abundant active sites, optimal Gibbs free energies for adsorption of intermediates

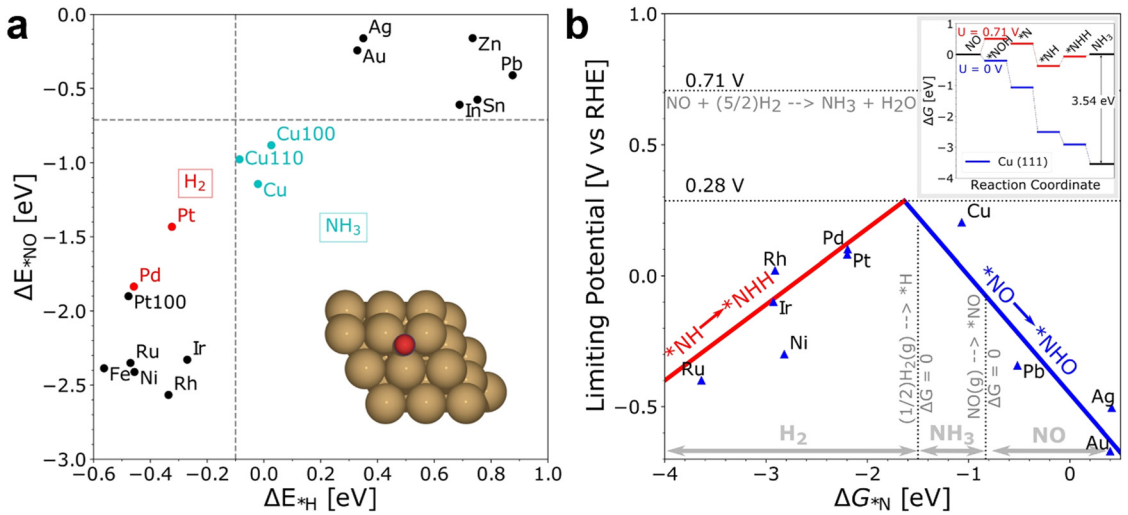

Fig. 3 (a) The adsorption energies of the intermediates ΔE^*_{NO} are plotted against ΔE^*_H on various metal surfaces. (b) The limiting potential volcano plot for NO reduction to NH_3 on various metal surfaces. Reproduced with permission from ref. 43 copyright 2021, Wiley-VCH.

to attain high ammonia (NH_4^+) yield rates, and high FEs at lower overpotentials.

For instance, Yu and co-workers have prepared Ru nanosheets with low coordination numbers (Ru-LCN) through the plasma treatment of Ru nanosheets with a high coordination number (Ru–HCN) (Fig. 4a).[71] As shown in Fig. 4b, Ru-LCN possesses enhanced NORR activity as compared to Ru-HCN in 1% NO (99% argon)-saturated 0.5 M Na_2SO_4 electrolyte. At an optimal potential of −0.2 V *vs.* RHE, Ru-LCN achieved a high NH_4^+ yield rate (45.03 μmol h^{-1} mg^{-1}) and FE (65.96%) in a H-type electrolytic cell (Fig. 4c). Moreover, the FE remains unaltered when the feeding gas is replaced with 99.9% NO instead of 1% NO, which is beneficial to produce NH_3 with a wide range of pollutant concentrations. In addition, they demonstrated an improved NH_4^+ yield rate of up to 84.20 μmol h^{-1} mg^{-1} at −0.2 V *vs.* RHE by constructing a flow electrolyzer (cathode: Ru-LCN, feed gas: 1% NO). The combined *in situ* measurements and DFT results indicated that the NH_3 molecule formation over the Ru surface has occurred through the alternating-N mechanistic pathway. As shown in Fig. 4d, the low coordination number of Ru not only helps in the NO* adsorption onto the Ru surface but also facilitates the subsequent hydrogenation step (PDS) *i.e.*, NO* to HNO*, thereby enhancing the NORR performance. However, the yield rate of Ru-LCN is not sufficiently high to meet the practical ammonia production rate. Recently, Lu *et al.* observed enhancement in the NORR activity of Ru active sites through the electronic structure optimization by forming an RuGa intermetallic compound (RuGa IMC).[72] Furthermore, RuGa nanoparticles were anchored onto the three-dimensional interconnected n-doped reduced graphene oxide nanosheets to improve the reaction kinetics *via* thermal annealing. Interestingly, the incorporation of Ga into Ru has altered the crystal structure from fcc-Ru to bcc-RuGa in which the isolated Ru atoms are occupied at the center of cubes (Ga atoms occupied at the vertex) (Fig. 4e). Meanwhile, an electron-rich Ru atom has been created through the electron transfer from Ga to Ru in RuGa IMC (Fig. 4f). As shown in Fig. 4g and h, bcc-RuGa exhibits an extraordinary NORR performance (NH_4^+ yield rate: 320.6 μmol h^{-1} mg^{-1}_{Ru} and FE: 72.3%), which is superior to that of fcc-Ru (yield rate: 235.4 μmol h^{-1} mg^{-1}_{Ru}, and FE: 59.8%) in 20% NO-saturated 0.1 M K_2SO_4 at −0.2 V *vs.* RHE. In another report, Shi *et al.* also showed higher intrinsic NORR activity of the $Ru_{0.05}Cu_{0.95}$ alloy prepared through the coprecipitation of $Ru_xCu_{1-x}(OH)_2$, followed by an electrochemical reduction step.[73] Online differential electrochemical mass

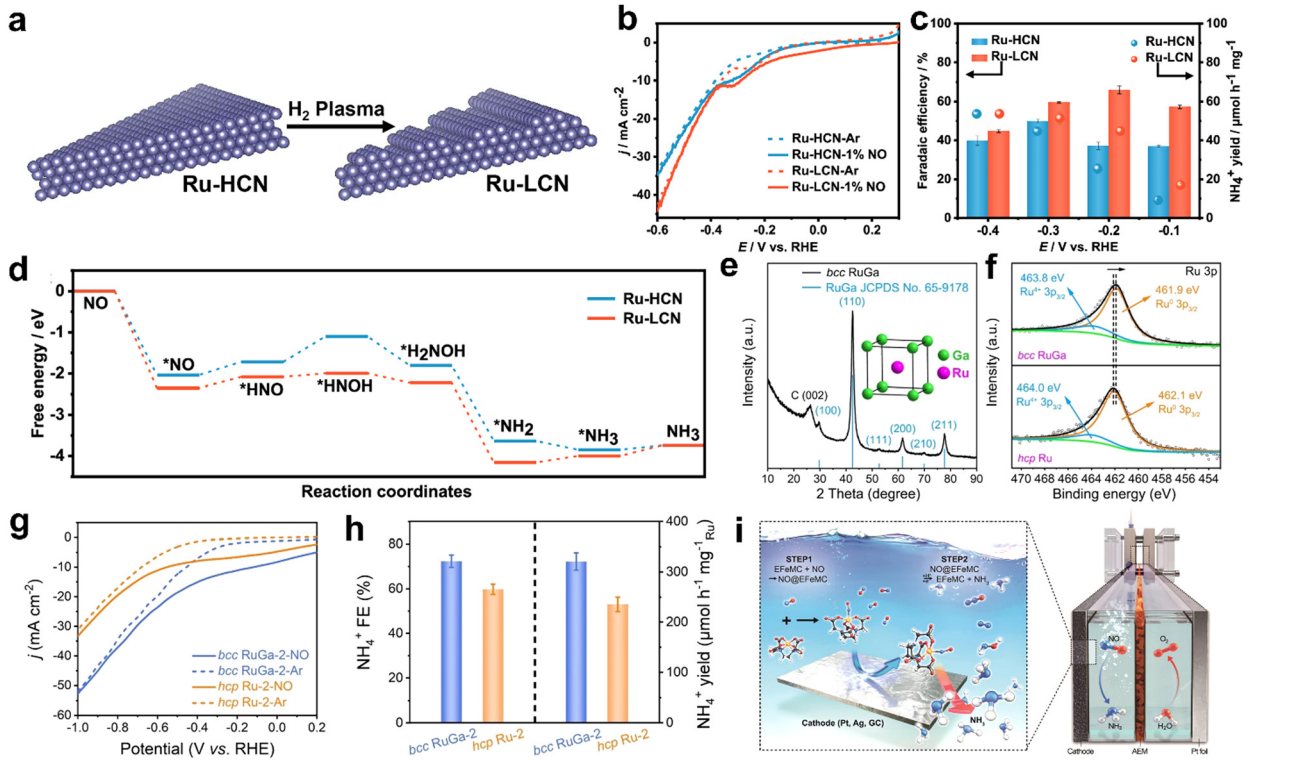

Fig. 4 (a) Diagram for the preparation of Ru-LCN *via* plasma treatment on Ru-HCN, (b) LSV curves of Ru-HCN and Ru-LCN at a scan rate of 10 mV s^{-1} in Ar- and 1% NO-saturated 0.5 M Na_2SO_4 solution, (c) Faradaic efficiency and yield rate of NH_4^+ with 1% NO over Ru-HCN and Ru-LCN at each given potential, and (d) reaction Gibbs free energy diagrams of the NORR over Ru-HCN and Ru-LCN on FCC (111) surfaces at 0 V *vs.* RHE. Reproduced with permission from ref. 71 copyright 2022, ACS. (e) XRD pattern of bcc RuGa IMCs on N-rGO nanosheets, the inset is the crystal structure (unit-cell) model of bcc RuGa IMCs, (f) high-resolution Ru 3p XPS spectra of bcc RuGa IMCs and hcp Ru NPs, (g) LSV curves of bcc RuGa-2 IMCs and hcp Ru-2 NPs in Ar-saturated (dashed lines) or NO-saturated (solid lines) 0.1 M K_2SO_4 electrolyte, and (h) NH_4^+ Faradaic efficiencies and NH_4^+ yield rates over bcc RuGa-2 IMCs and hcp Ru-2 NPs at 0.2 V in NO-saturated 0.1 M K_2SO_4 electrolyte. Reproduced with permission from ref. 72 copyright 2023, Wiley-VCH. (i) Schematic diagram showing NO capture by EFeMC present in the electrolyte and its electrochemical reduction to ammonia. Reproduced with permission from ref. 74 copyright 2020, ACS.

spectrometry (DEMS) confirms that ammonia (NH_3) is formed over the alloy through the alternating-N mechanistic pathway. Besides, Kim *et al.* have achieved the selective NH_4^+ formation using a nanostructured silver (Ag) electrode with nearly 100% FE in a large potential window (0.04 to −0.34 V *vs.* RHE) by using an EDTA-Fe^{2+} metal complex (EFeMC) electrolyte that is saturated with 'NO'.[74] They claimed that initially the 'NO' molecule gets trapped in the metal complex and subsequent proton-coupled electron transfer from the silver electrode to the metal complex occurs through the outer sphere electron transfer to produce NH_3 along with the regeneration of EFeMC (Fig. 4i). During electroreduction, Ag stabilizes the reaction intermediates such as [*(II)-HNO, *(II)-NHOH, and *(II)-NH_2OH, where *(II) = EFeMC] through donor–acceptor interaction by binding with the oxygen atoms of intermediates, which are trapped in the metal complex. In addition, the performance and durability of the Ag electrode are tested in a flow cell with the EFeMC electrolyte. In the flow cell, the NH_4^+ production rate has reached as high as 3.6 mol m^2 h^{-1}, along with 100% FE at −0.165 V *vs.* RHE and the same performance has been maintained for 100 h. Since they have used an additional metal complex in the electrolyte, it is especially important to estimate the economy of the system as compared to the commercial ammonia production cost. The economic analysis suggests that the NH_3 production cost through the NORR in the EFeMC-designed electrolyte is 2.5 times higher than the commercial price of ammonia but can be market competitive with an electricity price of \$0.03 kW h^{-1} and with a current density of >125 mA cm^{-2}. Thus, designing efficient electrocatalysts and integrating the electrolyzer with renewable energy sources could be a viable solution for implementing the EFeMC-electrolyte based NORR electrolyzer. In another report, Choi *et al.* have shown a notable NORR performance from commercial 20 wt% Au supported on Vulcan carbon to produce NH_4^+ at a relatively lower overpotential (−0.3 V), whereas the electrode is inert towards the NRR.[75] Xiong *et al.* reported improved NORR activity from electrochemically synthesized Au/rGO electrodes. Ferrous citrate (Fe^{II}Cit) solution was chosen as an electrolyte for the 'NO' complexation.[76] The NH_3 yield of Au/rGO increased linearly with the concentration of Fe^{II}Cit in the electrolyte, while maintaining the same FE. This indicates that the coordinated NO within the metal complex can only participate in electroreduction, which could solve the limited solubility problem of 'NO' in the aqueous electrolyte. Meanwhile, they observed that the FE of NH_3 can be maximized up to 98% with the adjustment of electrolyte pH to 1, as the key pronation step of *NOH is more facile in an acidic medium. Furthermore, they hypothesized that selective NH_3 formation over the Au surface is due to the stabilization of *N and *NH intermediates. At −0.47 V *vs.* RHE, an excellent NH_4^+ yield rate of 438.8 μmol cm^{-2} h^{-1} and FE of 93.2% were achieved from 7.6 wt% atomically dispersed iridium (Ir) confined in amorphous MoO_3 (Ir/MoO_3).[77] In this material, the Ir–O_5 moiety is found to be the active site for preferential binding of 'NO' over 'H' and possesses a very low energy barrier (0.01 eV) for the rate determining *NHO → *NHOH step, thereby delivering the high NH_3 yield rates and FE. Table 1 summarizes the NORR activity of different precious transition metal-based electrocatalysts.

2. Non-precious transition metal-based electrocatalysts

(i) Zero valent transition metals. Despite the high NORR performance of precious metals, their utilization for large-scale NH_3 production is hindered by the low abundance and high electrode cost. This demands the exploration of other alternatives for realizing the practical implementation of the NORR to NH_3 technology. In this context, Long *et al.* have performed computational screening over different transition metal catalysts towards NORR by choosing the N* adsorption free energy [G_{ad}(N)] as an activity descriptor.[34] Among the chosen transition metals, copper (Cu) is found to be the ideal candidate for selective NH_3 production through the NORR (Fig. 5a). In addition, the NH_3 formation over the Cu (111) surface is predicted to occur *via* an associative Heyrovsky distal-O mechanism (AHDO), in which the protonation of NOH* (0.54 eV) is the rate-limiting step. As shown in Fig. 5b, the high energy barriers for N–N, N–NO, and H–H couplings, as compared to N* continual protonation steps over Cu (111), have successfully eliminated the formation of N_2, N_2O, and H_2 side products, thereby leading to high activity and selectivity towards NH_3 production. They have validated the above predictions by performing electrocatalytic NORR experiments on copper substrates. A porous Cu foam has shown excellent NORR activity to produce NH_3 as a dominant product in a wide potential range from −1.2 to 0.3 V *vs.* RHE in 0.25 M Li_2SO_4 (Fig. 5c). A maximum NH_3 formation rate of about 517 μmol cm^{-2} h^{-1} along with high FE (93.5%) was achieved at −0.9 V *vs.* RHE and the activity was maintained for 100 hours. In contrast, hardly

Table 1 Summary of the NORR activity shown by different precious transition metal-based electrocatalysts

Catalyst	Synthetic route	Electrolyte	NH_3 yield rate	FE (%)	Potential (*vs.* RHE) (V)	Ref.
Ru-LCN	Plasma treatment	0.5 M Na_2SO_4 (1% NO)	45.03 μmol h^{-1} mg^{-1}	65.96	−0.2	71
RuGa IMCs	Thermal annealing method	0.1 M K_2SO_4 (20% NO)	320.6 μmol h^{-1} mg^{-1}_{Ru}	72.3	−0.2	72
$Ru_{0.05}Cu_{0.95}$	Coprecipitation–electrochemical reduction	0.5 M Na_2SO_4 (20% NO)	17.68 μmol h^{-1} cm^{-2}	64.9	−0.5	73
Nanostructured Ag electrode	Chlorination/dechlorination method	PBS-EDTA-Fe^{2+} metal complex (99.9% NO)	2.29 mol h^{-1} m^{-2}	~100	−0.34	74
20 wt% Au/C	Commercial	0.5 M K_2SO_4 (1 mM NO)	$8.1 \pm 0.9 \times 10^2$ pmol s^{-1} cm^{-2}	N. A.	−0.30	75
Au/rGO	Two-step electrochemical reduction	Citrate–Fe^{2+} complex (2% NO)	14.6 μmol h^{-1} cm^{-2}	65.2	−0.1	76
Ir/MoO_3	Supercritical CO_2 approach	NO-saturated 0.5M Na_2SO_4 (99.9% NO)	439 μmol h^{-1} cm^{-2}	93.2	−0.47	77

any NH_3 is formed when the Cu foam electrode is subjected to the NRR, thereby indicating the competitiveness of the NORR over the NRR on the Cu surface. Later, Chen *et al.* used the chemical reduction method for uniform decoration of ultra-small 'Cu' nanoparticles onto the porous TiO_2, which was synthesized by the sol–gel method.[78] The electrode exhibited a high NH_3 yield of 3520.80 μg h^{-1} mg^{-1} and FE of 86.49% at −0.3 V *vs.* RHE in 'NO'-saturated 0.1 M K_2SO_4. The improved surface area and porous channels of TiO_2/Cu have improved the 'NO' molecule adsorption, leading to high NH_3 production. Nevertheless, the poor solubility of NO_x in electrolytes is another roadblock to further development. This necessitates evaluating the NORR activity of electrocatalysts in a flow cell configuration by supporting them onto gas diffusion electrodes (GDEs) to alleviate the mass transport limitation. Ko *et al.* have demonstrated the gaseous NO_x (NO and N_2O) reduction at high reaction rates (400 mA cm^{-2}) over various transition metals deposited on GDEs in a gas-fed three-compartment flow cell.[57] In contrast to the previous reports, all the transition metals showed good electrocatalytic performance towards the NORR, while the product selectively is hugely varied (Fig. 5d). The higher activity shown by all metals could be due to the NO-saturated environment in the flow cell (100% NO). Among all the metals, Cu showed excellent selectivity (>80%) towards NH_3 from the NORR, whereas other metals, such as Fe, and Pd, have produced N_2O as a major product in an alkaline medium (Fig. 5e). Besides, Cu also showed good N_2ORR activity and it has selectively produced N_2 as a reduction product. In addition, they have studied the effect of NO partial pressure in a flow cell on product selectivity. It was found that irrespective of the electrocatalyst, N–N coupled products (N_2 and N_2O) and single-N products (NH_3 and NH_2OH) will be formed at low and high 'NO' coverages, respectively, thereby indicating the importance of the NO concentration over the catalyst surface towards product selectivity (Fig. 5f and g). In addition, they showed the pH dependency of the NORR towards NH_3 FE over Cu. It could deliver nearly 100% FE at pH = 0.5, as the first proton transfer step of NO (*NO + H^+ ↔ *NOH) is the rate determining step (RDS) of NH_3. Besides, NH_3 production from low concentrated 'NO' is of practical significance, especially while using flue gas as a NO source in the flow cell. Cheon *et al.* also reported excellent NORR activity from zero valent iron (Fe)-incorporated carbon black, which is supported on GDE at low NO concentrations (1–10%).[79] As shown in Fig. 5h, Fe/C-

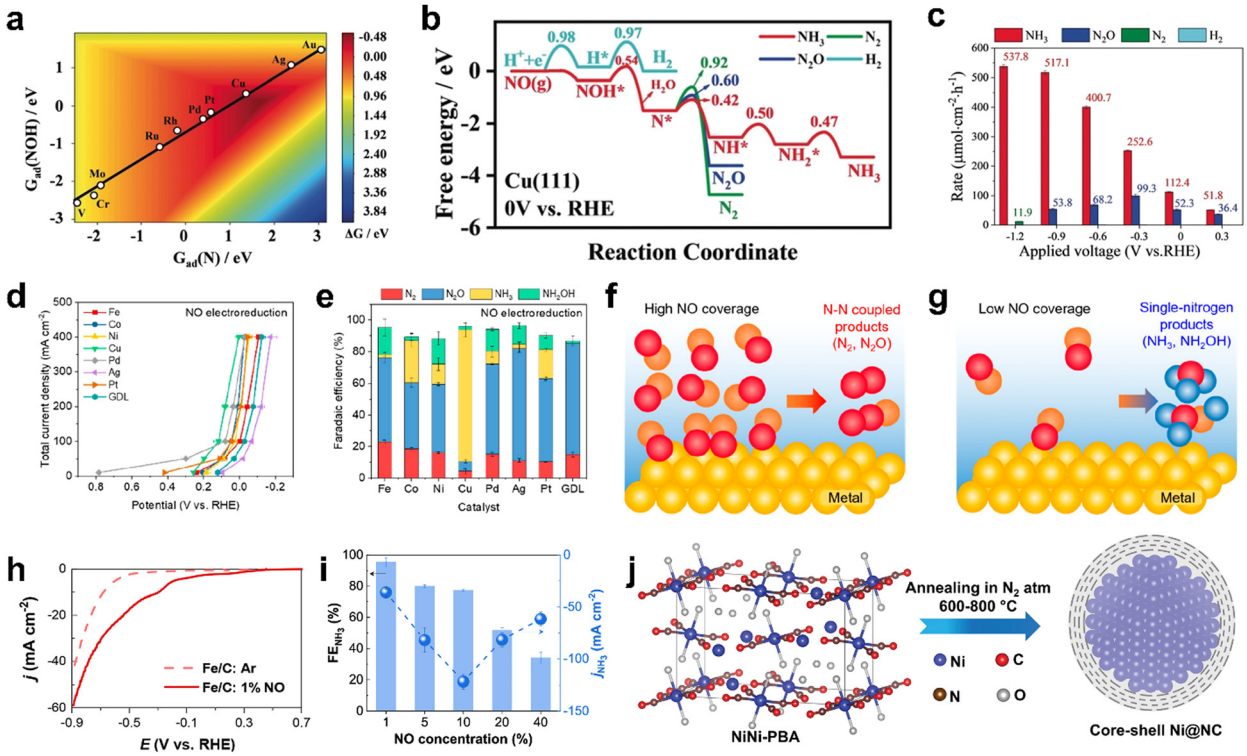

Fig. 5 (a) A two-dimensional activity map of different metals for ammonia production. All the reaction free energies are shown at 0 V *vs.* RHE, (b) free-energy diagrams for the HER, NORR to NH_3, N_2O, and N_2 over Cu (111) under 0 V *vs.* RHE, the kinetic barriers are shown in eV, and (c) reaction rates of the NORR on Cu foam at various potentials. Reproduced with permission from ref. 34 copyright 2020, Wiley-VCH. (d) Total current density *vs.* potential plots of various metal catalysts towards NO electroreduction performance, (e) Faradaic efficiency of various catalysts at 0.10 ± 0.02 V *vs.* RHE for NO electroreduction, and (f and g) schematics showing the effect of NO coverage on product selectivity in high and low NO coverages. Reproduced with permission from ref. 57 copyright 2022, ACS. (h) Linear sweep voltammetry scan of the Fe/C-incorporated GDE cell for 1% NO reduction using 0.5 M PBS electrolyte (pH 7), (i) the effect of NO concentration on NH_3 faradaic efficiency and NH_3 partial current density in a NO electrolyzer operated at −0.6 V *vs.* RHE and 0.5 M PBS (pH 7). Reproduced with permission from ref. 79 copyright 2022, ACS. (j) Schematic synthesis route of Ni@NC from NiNi-PBA. Reproduced with permission from ref. 40 copyright 2022, Wiley-VCH.

supported GDE has achieved a maximum FE_{NH_3} of 91% at −0.4 V *vs.* RHE and j_{NH_3} of 19 mA cm^{-2} at −0.6 V *vs.* RHE, respectively, with 1% NO as a feed gas in a GDE cell. In addition, a maximum j_{NH_3} of 122 mA cm^{-2} was achieved at 10% NO (FE: 77%). A further increase in the NO concentration led to a decrease in j_{NH_3} and FE, owing to the formation of N–N coupled products (N_2 and N_2O) at high 'NO' coverage over the electrode surface (Fig. 5i). The computational calculations revealed that the ammonia formation over the Fe (110) surface occurred through the breaking of the N–O bond in the H_2NO intermediate. Although the NH_3 yield rate of Fe/C-supported GDE is significantly improved in 0.5 M H_2SO_4 compared to PBS buffer, the dissolution of Fe in an acidic medium causes a decline in activity during long term NO electrolysis. The above studies show that the NH_3 production rate is significantly higher in the acidic medium than in neutral and alkaline electrolytes, owing to the facile protonation steps in the acidic medium. However, transition metals tend to dissolve in acidic environments, which causes catalyst degradation. Hence, it is necessary to protect the catalytic metal centers for durable ammonia production. To resolve this issue, our group attempted to protect catalytic Ni centers with a thin graphitic carbon coating by making a core–shell Ni@NC architecture *via* one-step pyrolysis of the $Ni[Ni(CN)_4]$ PBA precursor at different temperatures from 600 to 800 °C (Fig. 5j).[40] Among them, Ni@NC synthesized at 800 °C produced the highest NH_3 yield rate of 34.6 μmol cm^{-2} h^{-1} with a high FE (72.3%) at a low overpotential of 550 mV (0.16 V *vs.* RHE) and maintained the catalytic activity for 24 h in 0.1 M HCl. In contrast, bare Ni nanoparticles displayed a moderate NH_3 yield rate (8.9 μmol cm^{-2} h^{-1}) and they were etched away from the electrode surface during the NORR measurements. The improved activity of Ni@NC is attributed to the facile ionic/gaseous transport through the porous multilayer NC shell to the catalytically active Ni core. In addition, the anti-corrosive property of the multilayer NC shell retards the dissolution of the Ni core in an acidic medium, thereby ensuring the stability of Ni@NC. Furthermore, a solar powered NORR/OER electrolyzer (constructed by employing Ni@NC and RuO_2 as the cathode and anode, respectively) has achieved a NH_3 FE of > 50%, with a solar-to-fuel (STF) efficiency of ≈1.7%. Another work observed a stable NORR performance from N-doped carbon-wrapped nickel nanoparticles supported onto the carbon fiber (NiNC@CF).[80] Initially, nanoflake-like Ni-MOF was directly grown onto the CF *via* a solvothermal method. The subsequent thermal pyrolysis led to the decomposition of organic matter, producing a zero-valent Ni nanoparticle-dispersed porous N-doped carbon microstructure on CF. The resulting electrode achieved a maximum FE of 87% with an NH_3 yield rate of 94 mmol cm^{-2} h^{-1} at −0.5 V *vs.* RHE and showed good durability in the PBS electrolyte (pH 7). Meanwhile, the corresponding prototype two-electrode electrolyzer (NORR/OER) has delivered a NH_3 yield rate of 27 mmol cm^{-2} h^{-1} with the highest FE (80%), at a cell potential of 2.75 V. Wang and coworkers have attained a high NH_3 yield of 439.5 μmol cm^{-2} h^{-1} (1465.0 μmol h^{-1} mg_{cat}^{-1}) and an FE of 72.58% at −0.6 V *vs.* RHE from the hexagonal-close-packed cobalt nanosheets (hcp-Co) prepared through a facile hydrothermal method.[81] In contrast, the face-centered cubic phase of the Co nanosheets (fcc-Co) showed inferior activity (NH_3 yield: 142.10 μmol cm^{-2} h^{-1} and FE: 57.12%), thereby indicating that the crystal structure/phase of the material has a significant role in the NORR. The DFT studies unveil that hcp-Co activates the adsorbed 'NO' molecule through the donation of 0.6 e^- through d–π* orbitals and facilitates the rate determining first protonation step (NO* → NOH*) with a low energy barrier of 0.32 eV. Despite both hcp-Co and fcc-Co possessing a similar energy barrier for the RDS, the proton diffusion/shuttling is highly favourable over hcp-Co (−0.80 eV) as compared to fcc-Co (−0.67 eV). Hence, the improved activity of hcp-Co could be attributed to the expedited protonation kinetics during the NORR. Table 2 summarizes the NORR activity of different zero valent non-precious transition metal-based electrocatalysts.

(ii) Multi-valent transition metal compounds. The NORR activity and the NH_3 selectivity hugely depend on the electronic structure, morphology, and vacancies of electrocatalysts. In this regard, various metal compounds, such as oxides, sulfides, and phosphides, have been explored and it is found that all the materials can perform NORR activity with high NH_3 selectivity. As the biological reduction of NO into N_2O is catalyzed by an iron-centered heme group of 'NO reductase' Fe-based electrocatalysts are expected to show good 'NO' binding and perform the subsequent reduction.[83–85] Sun *et al.* have directly grown a uniform Fe_2O_3 nanorod array onto a 3-dimensional carbon paper (Fe_2O_3/CP) and evaluated its NORR activity with diluted NO (10%).[86] In addition, to improve the 'NO' solubility, they introduced Fe(II)EDTA complex into the 0.1 M Na_2SO_4 electrolyte. Fe_2O_3/CP has shown a good NH_3 yield of 41.6 μmol h^{-1} cm^{-2} (FE: 86.73%) at −0.4 V *vs.* RHE and maintained the activity for 12 h. Meanwhile, they found that NO_3^- contamination (resulting from the reaction between NO and O_2 followed by the dissolution in water) in the electrolyte causes interference of cathodic currents, thereby hindering the NORR activity judgment of electrodes. Hence, it is necessary to perform NORR in gas-tight (without the aeration of NO) cells to obtain reliable results. Besides, they demonstrated the NH_3 production (145.28 mg h^{-1} mg_{cat}^{-1}) at a high-power density (1.18 mW cm^{-2}) from the Zn–NO battery, which is assembled using Fe_2O_3/CP and a zinc plate as the cathode and anode, respectively. DFT studies predict that 'NO' strongly binds onto the Fe_2O_3 (104) surface through an ''acceptance–donation'' mechanism and subsequently gets activated through the 2p* back-donation effect to give rise to NH_3 molecule formation. The same group has shown boosted NORR activity using an oxygen vacancy (V_O)-rich MnO_2 nanowire array (MnO_{2-x} NA) supported on a Ti mesh in 0.2 M Na_2SO_4.[87] The V_O in MnO_{2-x} NA is created by annealing the as prepared MnO_2 NA in an Ar atmosphere at 350 °C. MnO_{2-x} NA has achieved a high NH_3 yield (27.51×10^{-10} mol s^{-1} cm^{-2}) and FE (82.8%) as compared to pristine MnO_2 NA (8.83×10^{-10} mol s^{-1} cm^{-2}, 44.8%) at −0.7 V *vs.* RHE, thereby highlighting the advantage of V_O in MnO_{2-x} for enhanced NORR activity. DFT calculations reveal that the hydrogenation step of MnO_2 (211) is associated with a high energy barrier due to the strong binding (−1.4 eV) of 'NO'. In contrast, V_O in the MnO_{2-x} (211) surface allows the moderate binding

Table 2 Summary of the NORR activities shown by different zero valent non-precious transition metal-based electrocatalysts

Catalyst	Synthetic route	Electrolyte	NH_3 yield rate	FE (%)	Potential (*vs.* RHE) (V)	Ref.
Cu foam	Commercial	0.25 M Li_2SO_4 (30 ml min^{-1})	517.1 μmol cm^{-2} h^{-1}	93.5	−0.9	34
TiO_2/Cu	Sol–gel followed by chemical reduction	0.1 M K_2SO_4 (10% NO)	3520.80 μg h^{-1} mg^{-1}	86.49	−0.3	78
Cu Ti fibers	Air spraying	0.05 M Na_2SO_4 (10% NO)	400 μmol cm^{-2} h^{-1}	90	−0.6	82
Copper nanoparticles (GDE)	Commercial	0.1 M NaOH + 0.9 M $NaClO_4$ (100% NO)	1246 μmol cm^{-2} h^{-1}	78	0	57
Fe/C-incorporated GDE	Physical mixture of Fe and C	0.5 M PBS solution (10% NO)	908 μmol cm^{-2} h^{-1}	77	−0.6	79
Ni@NC	Pyrolysis of NiNi-PBA	0.1 M HCl (99.9% NO)	34.6 μmol cm^{-2} h^{-1}	72.3	0.16	40
NiNC@CF	Solvothermal + annealing	0.5 M PBS solution (pH 7) (99.9% NO)	94 mmol cm^{-2} h^{-1}	87	−0.5	80
hcp-cobalt nanosheets	Hydrothermal method	0.1 M Na_2SO_4	439.5 μmol cm^{-2} h^{-1}	72.58	−0.6	81

(−0.5 eV) of 'NO' molecules, which makes the subsequent hydrogenation step more facile. Similarly, an oxygen vacancy-rich TiO_2 nanoarray supported on a Ti plate (TiO_{2-x}/TP) has shown superior NORR activity compared to TiO_2/TP as the 'NO' adsorption is more facile in the former.[88] Encouragingly, an open nano array structure of TiO_{2-x}/TP enables the exposure of abundant active sites for generating greater NH_3 yields. Wu *et al.* have achieved an exceptionally high NH_3 yield rate of 20 mg h^{-1} cm^2 with nearly unit FE from $CoNi_{(5:5)}O_x$@Cu at −0.68 V *vs.* RHE.[89] Moreover, the material maintained its NORR activity for 36 h. The *in situ* Raman spectroscopic and DFT studies concurrently manifest that 'NO' most likely adsorbs onto the Co site of $CoNi_{(5:5)}O_x$@Cu more spontaneously as compared to individual Co_3O_4@Cu and NiO@Cu. Subsequently, NH_3 is selectively produced through the O-end distal pathway, as the energy barriers are significantly high for the formation of other products (N_2, H_2, N_2H_4, *etc.*). Besides, the confinement of reaction intermediates in nanoreactors is proven to be a prudent approach for efficient NORR. Bai *et al.* have developed a synthetic strategy to prepare hollow Cu_2O@-$CoMn_2O_4$ nanoreactors from a Cu_2O nanocube template through the simultaneous etching of Cu_2O and growth of CoMn-LDH followed by annealing in Ar (Fig. 6a).[90] Meanwhile, they found that the NO adsorption ability linearly increases with nanoreactor internal space, which can be controlled by the etching time (Fig. 6b and c). The void-confinement effect of the Cu_2O@-$CoMn_2O_4$ nanoreactors is beneficial to maintain high reactant concentration and intermediate confinement inside the nanoreactor space and improve the electron transfer efficiency. The optimized material Cu_2O@$CoMn_2O_4$-8 (etched for 8 min) has shown remarkable NORR activity with a high NH_3 production rate of 94.18 mmol g^{-1} h^{-1} and an FE of 75.05% at −0.8 V *vs.* RHE (Fig. 6d and e). Zhang *et al.* found that 2H-MoS_2 flakes grown on graphite felt (MoS_2/GF) can efficiently convert NO into NH_3 in an acidic electrolyte.[54] As shown in Fig. 6f and g, the electrode has shown a maximum NH_3 yield rate of 99.6 μmol h^{-1} cm^{-2} (FE_{NH_3} < 30%) at −0.7 V *vs.* RHE from the electrocatalytic NORR and the corresponding Zn–NO battery has achieved a power density of 1.04 mW cm^{-2} (an NH_3 yield of 411.8 μg h^{-1} mg_{cat}^{-1}). DFT studies unveiled that 'NO' adsorption on MoS_2 (101) occurs through an 'acceptance–donation mechanism' and the subsequent activation is enabled by the electron transfer from MoS_2 to the anti-bonding orbital of 'NO' (Fig. 6h). However, the competitiveness of the HER over the NORR on the MoS_2 surface at high cathodic potentials resulted in low FE_{NH_3}. To suppress the HER on MoS_2, Liu's group performed NORR in an ionic liquid (IL)-based electrolyte, which can significantly limit the proton concentration over the electrode surface.[91] They regulated the electronic structure of MoS_2 *via* phosphorous (P) doping to enhance the NH_3 yield. As expected, FE_{NH_3} on P-MoS_2 nanospheres in 1-butyl-1-methypyrrolidinium tris(pentafluoroethyl)-trifluoro phosphate increased up to 70% and achieved an NH_3 yield rate of 237.7 μg h^{-1} mg_{cat}^{-1} at −0.6 V *vs.* RHE, which is superior to that of pristine MoS_2. Additionally, the computational studies showed that the associated energy barriers from NO adsorption to NH_3 formation on the MoS_2 surface are significantly lowered after P-doping, which could be the reason for such an enhanced NH_3 yield from P-MoS_2. Besides doping, creating sulfur vacancies in metal sulfides is also proven to be an effective way to enhance the electrocatalytic NORR performance. The sulfur vacancy-rich CoS_{1-x} nanosheets prepared through the plasma treatment have shown an NH_3 yield rate of 44.67 μmol cm^{-2} h^{-1} (FE: 54%) at −0.4 V *vs.* RHE in 0.2 M Na_2SO_4.[92] The 'S' vacancy-free CoS counterpart could only display an NH_3 yield rate of 27.02 μmol cm^{-2} h^{-1} (FE: 37%), as it possesses low active site density (reflected from double layer capacitance (C_{dl}) measurements) as compared to CoS_{1-x}. In addition, the 'NO' activation barrier is found to be relatively lower on CoS_{1-x} (100) facets, which may be attributed to the localization of electrons around the sulfur vacancies.

Transition metal phosphides have also shown promising catalytic activity by catalyzing the NORR at relatively low onset potentials (about −0.01 V *vs.* RHE). However, the excellent NH_3 selectivity is limited to low overpotentials as the competitive HER prevails at larger cathodic potentials on metal phosphides. For instance, Mou *et al.* synthesized a Ni_2P nanosheet array supported on carbon paper (Ni_2P/CP) through the vapor phase phosphorization of the as prepared $Ni(OH)_2$/CP precursor (Fig. 7a and b).[93] As shown in Fig. 7c and d, Ni_2P/CC has achieved a maximum NH_3 yield of 33.47 μmol h^{-1} cm^{-2}, high FE up to 77% at −0.2 V *vs.* RHE in 0.1 M HCl saturated with 10% NO, and maintained good long-term stability for up to 12 h. The assembled Zn–NO battery using Ni_2P/CP as the cathode delivered a discharge power density of 1.53 mW cm^{-2} by producing an ammonia yield of 62.05 μg h^{-1} mg_{cat}^{-1}. Theoretical calculations indicate that two-way charge transfer occurs between Ni_2P (111) and NO, which can simultaneously accumulate and deplete the electron density in the antibonding and bonding orbitals of NO, respectively. Consequently, the N–O bond will

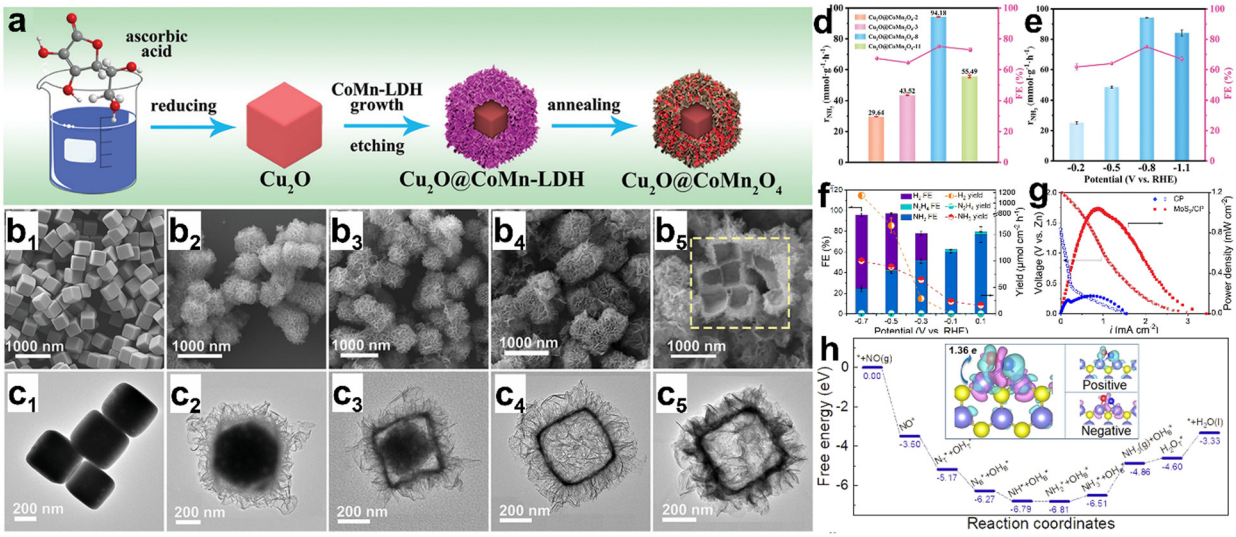

Fig. 6 (a) Schematic illustration of the preparation of a hollow $Cu_2O@CoMn_2O_{4-x}$ nanoreactor. SEM images of (b_1) Cu_2O, (b_2) $Cu_2O@CoMn_2O_4$-2, (b_3) $Cu_2O@CoMn_2O_4$-3, (b_4) $Cu_2O@CoMn_2O_4$-8 and (b_5) $Cu_2O@CoMn_2O_{4-x}$-11. TEM images of (c_1) Cu_2O, (c_2) $Cu_2O@CoMn_2O_4$-2, (c_3) $Cu_2O@CoMn_2O_4$-3, (c_4) $Cu_2O@CoMn_2O_4$-8 and (c_5) $Cu_2O@CoMn_2O_4$-11, (d) NH_3 production rate and selectivity of $Cu_2O@CoMn_2O_{4-x}$, and (e) NH_3 production rate and selectivity of $Cu_2O@CoMn_2O_4$-8. Reproduced with permission from ref. 90 copyright 2022, Wiley-VCH. (f) Product distribution for MoS_2/GF at each given potential in a NO-saturated 0.1 M HCl electrolyte containing 0.5 mM $Fe^{II}SB$, (g) polarization and power density plots of CP and MoS_2/CP, and (h) free energy landscape for NORR on MoS_2 (101). The charge density differences for the adsorbed NO are displayed as insets and cyan (positive) and red (negative) regions represent electron accumulation and loss, respectively. Reproduced with permission from ref. 54 copyright 2021, Wiley-VCH.

elongate and gets weaken on the Ni_2P (111) surface to facilitate the successive hydrogenation steps and produces NH_3 through the distal pathway (Fig. 7e). Similarly, CoP nanowire and FeP nanorod arrays are also revealed to be excellent candidates for catalyzing the NORR at low overpotentials, and both have achieved high FE_{NH_3} (88%) at −0.2 V *vs.* RHE in Na_2SO_4 and PBS electrolytes, respectively.[94,95] Transition metal carbides are another class of materials predicted to show a strong affinity towards NO adsorption owing to the good orbital overlap between d and p-orbitals of the metal and NO, respectively. This could facilitate the back-donation of electrons from metal centers to NO, activating the NO molecule to produce ammonia. Chu's group developed molybdenum carbide (Mo_2C) nanosheets by using methane gas as a carbon source through the carbonization of MoO_3 nanosheets at 700 °C.[96] As shown in Fig. 7f, Mo_2C nanosheets produced the main product NH_3 with a yield rate of 122.7 μmol h^{-1} cm^{-2} (FE_{NH_3}: 86.3%) at −0.4 V *vs.* RHE in Na_2SO_4 and the same efficiency is retained for continuous 20 h electrolysis. As shown in Fig. 7g–i, DFT studies verify the preferred adsorption of 'NO' over the 'H' atom on the Mo_2C surface and the subsequent electron transfer from the 'Mo' center to absorbed NO. Hence, the Mo_2C surface has helped to enhance the NORR and delivers high NH_3 selectivity by impeding HER kinetics. In another report, Liu and coworkers demonstrated stable NORR performance with high NH_3 selectivity from MoC nanocrystals confined in N-doped carbon nanosheets (MoC/NCS).[97] Carbon support is found to be beneficial for abundant active site exposure and accelerated electron transport. In addition, the corresponding Zn–NO battery exhibited a peak power density of 1.8 mW cm^{-2} and a large NH_3 yield rate of 782 ± 10 μg h^{-1} cm^{-2}. Furthermore, the potential determining step on the MoC (111) surface is predicted to be the hydrogenation of *NH, which is associated with a small energy barrier of 0.35 eV, leading to high NH_3 selectivity over the other side products (H_2, N_2, and N_2O). Table 3 summarizes the NORR activity of different multivalent non-precious transition metal compounds.

(iii) Transition metal-based single atom catalysts (SACs). Recently, SACs have evolved as promising materials for various electrocatalytic applications such as the HER and ORR/OER owing to their maximized atom-utilization efficiency.[102,103] Meanwhile, their NORR activity and product selectivity are hugely dependent on the coordination environment around the metal center.[104,105] For instance, Peng *et al.* have shown good NORR activity from single-atom Nb sites supported on B, N co-doped carbon nanotubes (Nb-SA/BNC) prepared through the pyrolysis of melamine foam that was soaked in a precursor solution consisting of Nb(v) oxalate hydrate, polyethylene glycol, urea, and boric acid (Fig. 8a).[106] The atomic dispersion of Nb atom sites over the amorphous carbon nanotubes is identified using a high-angle annular dark-field scanning transmission electron microscopy (HAADF-STEM) image (Fig. 8b and c). As shown in Fig. 8d, each Nb atom in Nb-SA/BNC is found to be coordinated with two B atoms and two N atoms to create the Nb-B_2N_2 unit. The 'NO' adsorption is predicted to occur on the Nb site through the d–π* orbital overlap and subsequently gets activated through the electron donation from the Nb atom. An appreciable NORR activity along with high NH_3 selectivity was noted from atomically dispersed cobalt (Co) single atoms onto the MoS_2 basal planes (Co/MoS_2).[107] It exhibited a maximum NH_3 yield and FE_{NH_3} of 217.6 μmol h^{-1} cm^{-2} and 87.7%, respectively, at −0.5 V *vs.* RHE and showed excellent durability for 15 h. X-Ray absorption fine structure (EXAFS) analysis confirms the atomic level dispersion of Co atoms and is coordinated with three surface S atoms of MoS_2 to

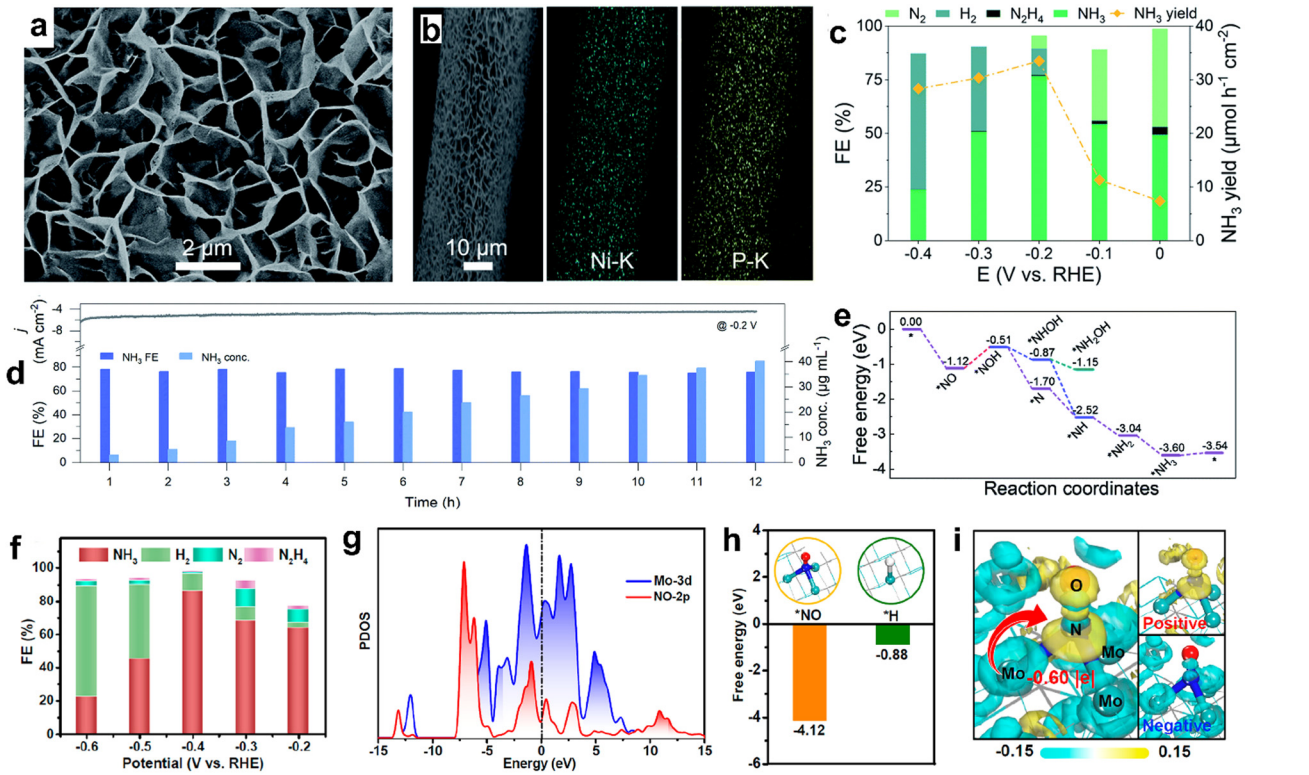

Fig. 7 (a) SEM image of Ni_2P/CP, (b) EDX elemental map of Ni_2P/CP, (c) FEs of the major reduction products and NH_3 yields for Ni_2P/CP, (d) long-term stability tests for continuous generation of NH_3 on Ni_2P/CP, and (e) free energy diagrams for the NORR on the Ni_2P (111) surface along the distal and alternating pathways. Reproduced with permission from ref. 69 copyright 2021, RSC. (f) FEs of Mo_2C at various potentials, (g) projected density of states (PDOS) profiles of adsorbed NO and its bonded Mo atoms, (h) comparison of *NO and *H adsorption on Mo_2C, and (i) electron density distributions of NO adsorption on Mo_2C (001). Reproduced with permission from ref. 96 copyright 2023, ACS.

form a Co–S_3 moiety, which is predicted to be the active site for NO reduction. In addition, they emphasized that during the NORR, the N═O bond activates through the electron donation from the Co–S_3 moiety, and the consecutive hydrogenation steps occur through the NHO pathway (*NO → *NHO → *NHOH → *NH_2OH→ *NH_2 → *NH_3). Similarly, Cu–S_3 moieties of the single-atomic copper supported on MoS_2 (Cu/MoS_2) also served as efficient catalytic centers for the NORR.[105] Meanwhile, the same group has used a combined strategy of atomic doping and vacancy engineering to improve the NORR activity of SACs.[108] They have prepared atomically Fe-doped and S-vacancy-rich MoS_2 (Fe/MoS_{2-x}) nanoflowers using a facile one-step hydrothermal method and achieved a high NH_3 yield rate of 288.2 μmol h^{-1} cm^{-2} (FE: 82.5%) at −0.6 V *vs.* RHE. EXAFS spectra of Fe K-edge and Mo K-edge confirm the existence of atomically distributed Fe dopants coordinated with lattice S atoms and the abundant sulfur vacancies (V_S) in Fe/MoS_{2-x} (Fig. 8e–h). In addition, the DFT calculations reveal that the cooperative effect of Fe-doping and V_S has facilitated the NO adsorption and activation on Fe–Mo dual sites (Fig. 8i). Furthermore, the high 'H' adsorption barrier on Fe–Mo dual sites of Fe/MoS_{2-x} has prohibited HER thereby resulting in high NH_3 selectivity (Fig. 8j). Table 4 summarizes the NORR activity of different Transition metal based single-atom catalysts.

3. p-Block element based electrocatalysts

The previous section showed that d-block element-based electrocatalysts show promising NO molecule adsorption and activation owing to their unoccupied d-orbitals. However, the unoccupied d-orbitals are also favorable for 'H' atom binding, facilitating the competing HER and hindering the NH_3 selectivity in a wide potential window.[111,112] In contrast, excellent NH_3 selectivity is expected from p-block element-based electrocatalysts as they exclusively bind to 'NO' rather than 'H'. Lin *et al.* achieved an excellent FE_{NH_3} of about 90% and a high NH_3 yield rate of 1194 μg h^{-1} mg^{-1}_{cat} at −0.5 V *vs.* RHE from Bi nano dendrites (Fig. 9a).[111] Moreover, a good FE_{NH_3} is maintained in a wide potential window of −0.3 V to −0.6 V. At the same time, the H_2 gas is only detectable at high cathodic potentials (Fig. 9b). In addition, the DFT calculations predict that 'NO' binds strongly over the Bi (012) surface as compared to the hydrogen atom, and subsequently gets activated through a two-way charge transfer mode thereby resulting in high NH_3 FE. Similarly, an outstanding FE_{NH_3} of 93% is observed at −0.4 V *vs.* RHE of Bi nanoparticles decorated onto the carbon nanosheet. The corresponding Zn–NO battery has produced a maximum NH_3 yield of 355.6 μg h^{-1} cm^{-2} at a discharge current density of 4 mA cm^{-2}. Sulfur vacancy (Vs)-rich SnS_{2-x} also showed an exceptional FE_{NH_3} of 90.3% (NH_3 yield rate: 78.6 μmol h^{-1} cm^{-2}) at a large cathodic potential of −0.7 V *vs.* RHE, as the HER is significantly suppressed over the SnS_{2-x} surface.[112] Compared to SnS_{2-x}, the SnS_2 counterpart showed an inferior NH_3 yield rate and FE_{NH_3}, thereby highlighting the advantage of the defect engineering strategy towards enhanced NORR. Theoretical computations unraveled that a V_S-

Table 3 Summary of the NORR activity shown by different multi-valent non-precious transition metal compounds

Catalyst	Synthetic route	Electrolyte	NH_3 yield rate	FE (%)	Potential (*vs.* RHE) (V)	Ref.
Fe_2O_3 nanorods	Hydrothermal + annealing in Ar	0.1 M Na_2SO_4 + 0.5 mM Fe(II)EDTA (10% NO)	41.6 μmol h^{-1} cm^{-2}	86.73	−0.4	86
MnO_{2-x} nanowires	Solvothermal + annealing in Ar	0.2 M Na_2SO_4 (10% NO)	27.51 × 10^{-10} mol s^{-1} cm^{-2}	82.8	−0.7	87
TiO_{2-x} nanoarray	Hydrothermal + H^+ exchange + annealing	0.2 M PBS (10% NO)	1233.2 μg h^{-1} cm^{-2}	~65	−0.7	88
$CoNi_{(5:5)}O_x$@Cu	Electrodeposition	1 M KOH	20 mg h^{-1} cm^{-2}	~100	−0.68	89
NiO nanosheets	Hydrothermal + calcination in air	0.1 M Na_2SO_4 + 0.5 mM Fe(II)EDTA (10% NO)	2130 μg h^{-1} cm^{-2}	90	−0.6	98
NiFe LDH nanosheets	Hydrothermal method	0.25 M Li_2SO_4 + 0.5 mM Fe(II)EDTA (99.99% NO)	112 μmol h^{-1} cm^{-2}	82	−0.7	99
Cu_2O@$CoMn_2O_4$ hollow nanoreactors	CoMn-LDH growth on Cu_2O nano-cube + annealing in Ar	0.1 M Na_2SO_4 (99% NO)	94.18 mmol g^{-1} h^{-1}	75	−0.8	90
MoS_2/GF	Hydrothermal method	0.1 M HCl + 0.5 mM iron(II) sodium benzoate (10% NO)	99.6 μmol cm^2 h^{-1}	<30	−0.7	54
P-doped MoS_2 nanospheres	Hydrothermal + heat treatment with NaH_2PO_2	0.1 M 1-butyl-1-methypyrrolidinium tris(pentafluoroethyl) trifluorophosphate (99.99% NO)	237.7 μg h^{-1} mg_{cat}^{-1}	69	−0.6	91
CoS_{1-x} nanosheet	Hydrothermal + plasma treatment	0.2 M Na_2SO_4 (10% NO)	44.67 μmol cm^{-2} h^{-1}	53.62	−0.4	92
Ni_2P nanosheets	Hydrothermal + vapor phase phosphorization	0.1 M HCl (10% NO)	33.47 μmol h^{-1} cm^{-2}	76.9	−0.2	93
CoP nanowires	Hydrothermal + vapor phase phosphorization	0.2 M Na_2SO_4 (10% NO)	47.22 μmol h^{-1} cm^{-2}	88.3	−0.2	94
FeP nanorods	Hydrothermal + vapor phase phosphorization	0.2 M PBS solution (10% NO)	85.62 μmol h^{-1} cm^{-2}	88.49	−0.2	95
Mo_2C nanosheets	Liquid exfoliation of MoO_3 + vapor phase carbonization	0.5 M Na_2SO_4 (99.99% NO)	122.7 μmol h^{-1} cm^{-2}	86.3	−0.4	96
MoC/NCS	Pyrolysis of a molybdenum complex and melamine	0.1 M HCl + 0.5 mM iron(II) sodium benzoate (99.99% NO)	1350 μg h^{-1} cm^{-2}	89	−0.8	97
Amorphous NiB_2	Reflux approach	0.5 M Na_2SO_4 (99.99% NO)	167.1 μmol h^{-1} cm^{-2}	90	−0.4	100
Nanoporous VN film	Vapor phase nitridation of V_2O_5	0.1 M HCl + 0.5 mM iron(II) sodium benzoate (99.99% NO)	1.05 × 10^{-7} mol cm^{-2} s^{-1}	85	−0.6	101

induced unsaturated Sn site in SnS_{2-x} donates about −0.6 electrons to the adsorbed 'NO' to cause the N═O bond elongation and activation, while the electron donation is restricted over the Sn site of pristine SnS_2. Additionally, the free energies for all protonation steps on SnS_{2-x} are lower than those of SnS_2 and the RDS in the former is $*NH_2 \rightarrow *NH_3$ with an uphill of 0.4 eV. Liang *et al.* have observed the efficient 'NO' activation on amorphous $B_{2.6}C$, which is enabled by the effective electron injection into NO ($\pi 2p^*$) from the B–C bond.[113] Given that, the amorphous $B_{2.6}C$ is sputtered onto a Ti plate-supported TiO_2 nanobelt array (a-$B_{2.6}C$@TiO_2/Ti) and found that the electrode can deliver a high NH_3 yield rate of 3678.6 μg h^{-1} cm^2 and a FE_{NH_3} of 87.6% at −0.9 V *vs.* RHE, which are far higher than those of $B_{2.6}C$/Ti and TiO_2/Ti (Fig. 9c and d). Meanwhile, the electrode maintained the same activity for up to 12 hours for bulk electrolysis. In addition, a maximum NH_3 yield of 1125.2 μg h^{-1} cm^{-2} was obtained for the corresponding Zn–NO battery at a discharge current of 10 mA cm^{-2}. Metal-free boron phosphide (BP) also delivered a high FE of 83.3% with an NH_3 yield rate of 96.6 μmol h^{-1} cm^2 at −0.7 V *vs.* RHE.[114] The DFT calculations indicate that both B and P atoms of BP can synergistically activate 'NO' through a strong p–p orbital overlap. In addition, the first hydrogenation step ($*NO \rightarrow *NHO$) is found to be the RDS with a low energy barrier of 0.68 eV over BP(111). A promising NORR activity is noted from antimony single atoms confined in amorphous MoO_3 (Sb/a-MoO_3) nanosheets (Fig. 9e).[115] In Sb/a-MoO_3, Sb exists in a +3valence state and is surrounded by five O atoms to form Sb_1–O_5 units, as is confirmed by the Sb K-edge XANES and EXAFS studies. As shown in Fig. 9f, Sb/a-MoO_3 has exhibited an excellent FE_{NH_3}, of about 92%, and a high NH_3 yield rate of 273.5 μmol h^{-1} cm^{-2} at −0.6 V *vs.* RHE in 0.5 M Na_2SO_4. The combined *in situ* electrochemical studies and theoretical calculations demonstrated that Sb/a-MoO_3 prefers to follow an alternating-N pathway (Fig. 9g–i). Nevertheless, the 'Sb' site possesses optimal binding free energy for *NO and unfavorable binding free energies for both $*H_2O$ and *H, thereby impeding the competing HER (Fig. 9j).

Meanwhile, atomically isolated, and unsaturated Sb sites located on Sb_2S_3 also showed a significant NH_3 yield rate and excellent FE_{NH_3} ~94% owing to the powerful 'NO' activation through the electron donation–back donation phenomenon and the selective 'NO' adsorption over H_2O/H.[116] Besides, metal-free carbon-based materials are also found to be promising candidates toward efficient electroreduction of NO into NH_3 in a neutral medium. For instance, a honeycomb like carbon nanofiber coated onto a carbon paper has achieved a high FE_{NH_3} and NH_3 yield of 88.33%, 22.35 μmol h^{-1} cm^{-2}, respectively, at −0.6 V *vs.* RHE and showed good durability for up to 10 h.[117] During the NORR, the interconnected nanocavities in the carbon fiber can effectively entrap the NO gas, after that, the electrochemically active –OH functional groups on the fiber can facilitate the NO reduction with a low energy input. Similarly, metal-free g-C_3N_4 nanosheets deposited onto carbon paper (CNNS/CP) also showed remarkable NORR performance.[118] In addition, the regulation of the interface microenvironment around the CNNS/CP electrode through hydrophobic treatment is found to be beneficial for the improved gas–liquid–solid triphasic interface. Therefore, the NO

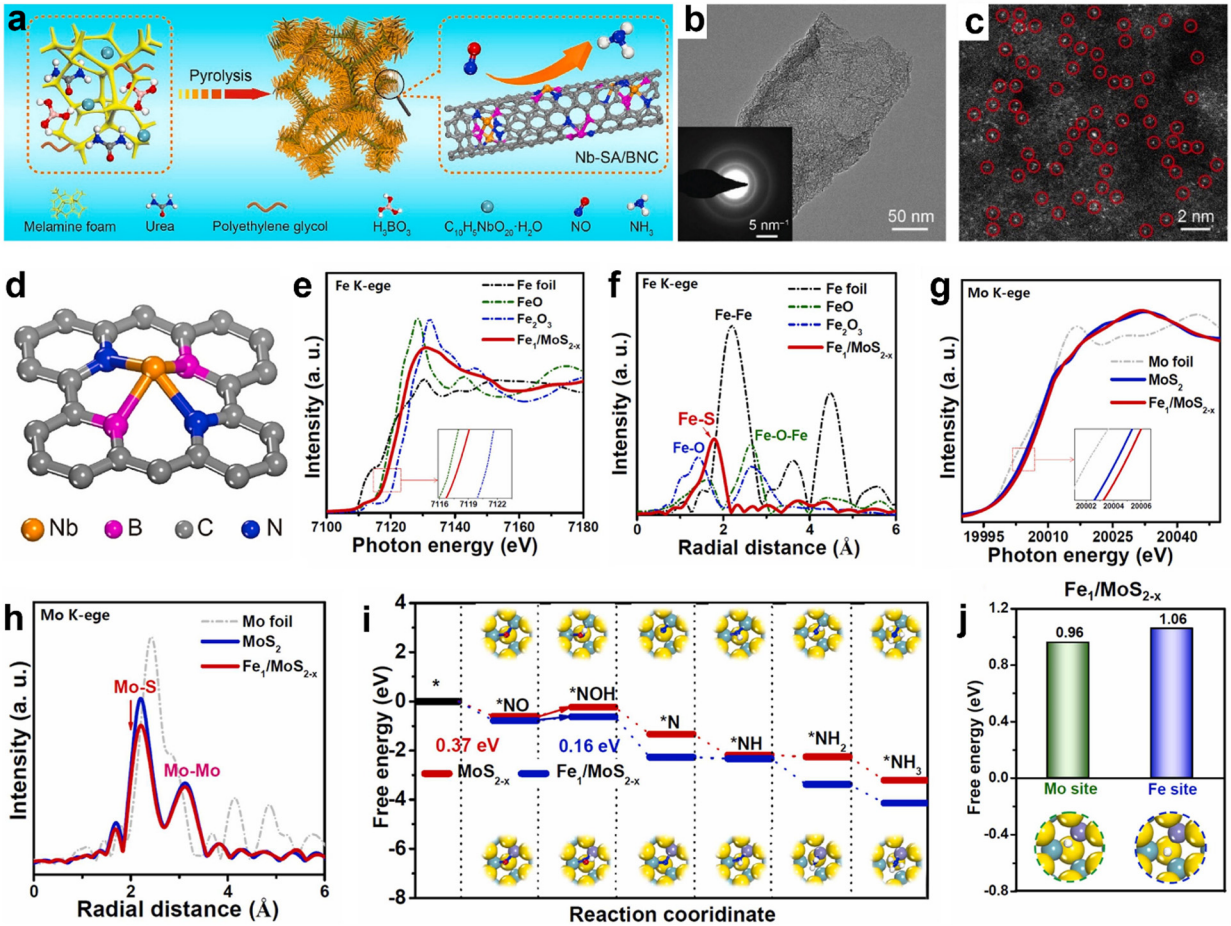

Fig. 8 (a) Schematic diagram of the synthetic procedure of Nb-SA/BNC, (b) TEM image and SAED pattern of Nb-SA/BNC (inset of Fig. 5b), (c) HAADF-STEM image of Nb-SA/BNC, in which some of the SA Nb sites are highlighted by red circles, and (d) atomic model of Nb-SA/BNC. Reproduced with permission from ref. 106 copyright 2020, Elsevier. Fe K-edge (e) XANES, and (f) EXAFS spectra of Fe/MoS_{2-x} and reference samples of Fe foil, FeO, and Fe_2O_3. Mo K-edge, (g) XANES and (h) EXAFS spectra of Mo foil, MoS_2, and Fe/MoS_{2-x}. (i) Free energy diagrams for the NORR on MoS_{2-x} and Fe/MoS_{2-x}, and (j) free energies of *H adsorption on MoS_2 and Fe/MoS_{2-x}. Reproduced with permission from ref. 108 copyright 2023, Elsevier.

Table 4 Summary of the NORR activity shown by different transition metal-based single-atom catalysts

Catalyst	Synthetic route	Electrolyte	NH_3 yield rate	FE (%)	Potential (*vs.* RHE) (V)	Ref.
Nb/BNC	Carbonization in Ar	0.1 M HCl (100% NO)	8.2×10^{-8} mol cm^{-2} s^{-1}	77	−0.6	106
Ce/NHCS	Impregnation + carbonization	0.05 M HCl + 0.5 mM iron(II) sodium benzoate (99.99% NO)	1023 μg h^{-1} mg$^{-1}_{cat}$	91	−0.7	109
W/MoO_{3-x}	Supercritical CO_2 approach	0.5 M Na_2SO_4 (99.99% NO)	~ 250 μmol h^{-1} cm^{-2}	91.2	−0.4	110
Co/MoS_2	Hydrothermal + impregnation method	0.5 M Na_2SO_4 (99.99% NO)	217.6 μmol h^{-1} cm^{-2}	87.7	−0.5	107
Cu/MoS_2	Hydrothermal + impregnation method	0.5 M Na_2SO_4 (99.99% NO)	337.5 μmol h^{-1} cm^{-2}	90.6	−0.6	105
Fe/MoS_{2-x}	Hydrothermal method	0.5 M Na_2SO_4 (99.99% NO)	288.2 μmol h^{-1} cm^{-2}	82.5	−0.6	108

mass transfer and availability over the electrode surface significantly increased, leading to 2 times enhancement in the NH_3 production. Table 5 summarizes the NORR activity of different p-block element-based electrocatalysts.

Perspectives and challenges

The research progress indicates that the electrocatalytic NORR has great potential to replace the conventional Haber–Bosch process for NH_3 production. However, the practical implementation of the NORR for NH_3 production is hindered by several challenges. First, most reported catalysts show high cathodic potentials (overpotentials) and exhibit unsatisfactory NH_3 yield rates and FE_{NH_3} values. Thus, developing efficient electrocatalysts with high NH_3 product selectivity is of paramount interest for reducing the cell potential in a commercial electrolyzer. In this context, strategies to modulate the electronic structure of the electrocatalysts through alloying, doping, and defect engineering

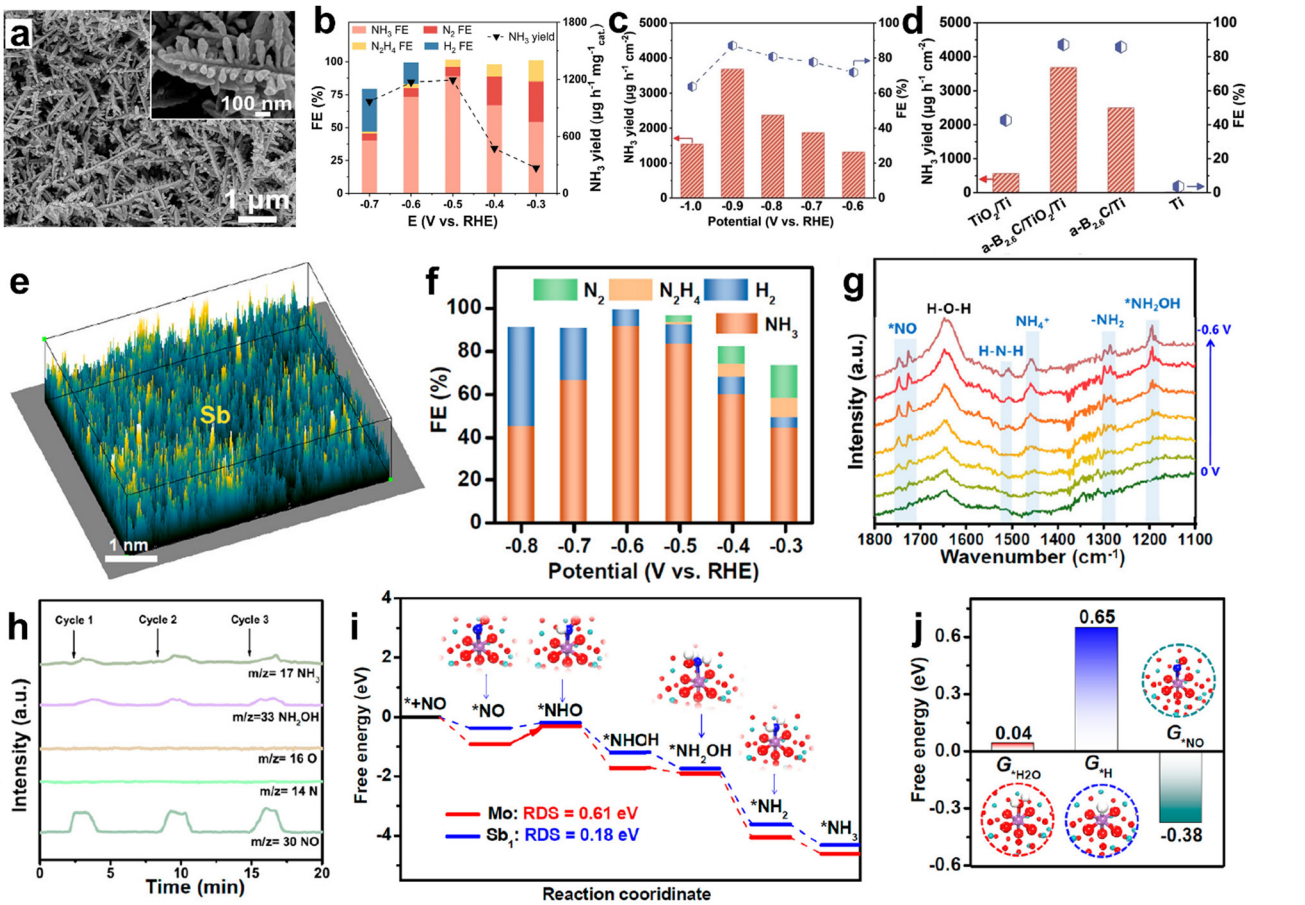

Fig. 9 (a) SEM image (inset: high-magnification image) of Bi NDs, (b) FEs of the major reductive products and NH_3 yields for Bi NDs/CP at each given potential. Reproduced with permission from ref. 111 copyright 2022, Elsevier. (c) FEs and NH_3 yields of a-$B_{2.6}C$@TiO_2/Ti at different potentials, (d) performance comparison. Reproduced with permission from ref. 113 copyright 2022, Wiley-VCH. (e) 3D atom image of p-block Sb single atoms confined in amorphous MoO_3 (Sb/a-MoO_3), (f) FEs of different products at various potentials, (g) potential-dependent *in situ* FTIR spectrum of Sb/a-MoO_3 from 0 to −0.6 V, (h) online DEMS spectrum of Sb/a-MoO_3 during the NORR electrolysis at −0.6 V, (i) free energy diagrams of alternating-N pathways on a-MoO_3 and Sb/a-MoO_3, and (j) binding free energies of *H_2O, *H, and *NO on Sb/a-MoO_3. Reproduced with permission from ref. 115 copyright 2023, ACS.

could be considered. The operando and computational studies also guide the designing of the catalysts with ideal crystal facets and compositions for selective 'NO' adsorption over 'H' and the subsequent NORR intermediate stabilization. In addition, the materials can be grown with unique morphologies, high surface area, and ideal porosity to improve the charge transport and active site density.

Second, most of the NORR studies have used expensive 100% NO gas as a source for NH_3 production as the solubility of 'NO' is poor in aqueous electrolytes (H-type cells). Although the utilization of 'NO' complexation agents in the electrolyte seems a promising strategy for attaining high NH_3 yield rates from dilute NO (10%), the additional cost of the reagent, recyclability, and the NH_3 separation from the electrolyte could be worrisome. In contrast, few studies have demonstrated that NH_3 can be produced from dilute NO (1–10% NO) through the gas phase electrolysis using gas diffusion electrodes (GDEs) coated with electrocatalysts in a flow cell configuration. Thus, to understand the feasibility of NH_3 synthesis from diluted 'NO' or exhaust gas, the NORR performance of the materials must be evaluated in the gas phase (GDE and flow cells) along with 'NO-saturated electrolytes' (in H-type cells) by using the diluted 'NO' reactant (1–10%). The catalysts should possess ideal Gibbs free energy and significant orbital overlap for 'NO' adsorption and the subsequent hydrogenation steps. Also, the gas phase electrolysis of diluted 'NO' could eliminate the formation of N–N coupled side products (N_2 and N_2O).

Third, the NORR measurements must be performed in gas-tight cells to obtain reliable results as there is a high probability of interference of cathodic currents from NO_3^- contamination. Furthermore, to identify the exact nitrogen source for NH_3 formation, ^{15}NO isotopic labelling experiments should be carried out. Despite most of the reports relying only on the colorimetric method for NH_3 quantification, the concurrent NMR measurements should be considered for further verification. DFT studies are used extensively to identify the active sites, Gibbs free energies for 'NO' and intermediate adsorption, RDS, and probable mechanistic pathways over different catalytic surfaces. However, the most favorable pathway of the NORR to NH_3 is still elusive as the results are hugely varied over the different crystalline planes

Table 5 Summary of the NORR activity shown by different p-block element-based electrocatalysts

Catalyst	Synthetic route	Electrolyte	NH_3 yield rate	FE (%)	Potential (*vs.* RHE) (V)	Ref.
Bi nanodendrites	Electrodeposition	0.1 M Na_2SO_4 + 0.5 mM Fe(II)EDTA (10% NO)	1194 μg h^{-1} mg^{-1}_{cat}	89.2	−0.5	111
Bi@C	Annealing of bismuth citrate	0.1 M Na_2SO_4 + 0.5 mM Fe(II)EDTA (10% NO)	1164.8 μg h^{-1} mg^{-1}_{cat}	93	−0.5	119
SnS_{2-x}	Hydrothermal + plasma treatment	0.5 M Na_2SO_4 (99.99% NO)	78.6 μmol h^{-1} cm^{-2}	90.3	−0.7	112
$B_{2.6}C$@TiO_2	Magnetron sputtering of $B_{2.6}C$ onto TiO_2	0.1 M Na_2SO_4 + 0.5 mM Fe(II)EDTA (10% NO)	3678.6 μg h^{-1} cm^{-2}	87.6	−0.9	113
BP	Vacuum-sealing approach	0.5 M Na_2SO_4 (99.99% NO)	96.6 μmol h^{-1} cm^{-2}	83.3	−0.7	114
Sb/a-MoO_3	Supercritical CO_2 approach	0.5 M Na_2SO_4 (99.99% NO)	273.5 μmol h^{-1} cm^{-2}	91.7	−0.6	115
In/a-MoO_3	Supercritical CO_2 approach	0.5 M Na_2SO_4 (99.99% NO)	242.6 μmol h^{-1} cm^{-2}	92.8	−0.6	120
Sb/Sb_2S_3	Solvothermal method	0.5 M Na_2SO_4 (99.99% NO)	168.6 μmol h^{-1} cm^{-2}	93.7	−0.7	116
Honeycomb carbon nanofiber	Electrospinning followed by carbonization	0.2 M Na_2SO_4 (10% NO)	22.35 μmol h^{-1} cm^{-2}	88.3	−0.6	117
g-C_3N_4 nanosheets	Calcination of melamine + ultrasonication	0.1 M PBS solution (20% NO)	30.7 μmol h^{-1} cm^{-2}	45.6	−0.8	118

and compounds. This makes it difficult to predict the ideal catalytic surfaces for efficient NORR to NH_3. Along with the computational studies, the real-time FTIR and DEMS studies could be beneficial to identify the reaction intermediates and to understand the favorable mechanism.

Fourth, the NORR performance of many reported electrocatalysts was evaluated in neutral and alkaline media. However, to obtain NH_3 from commercial PEM electrolyzers, efficient and durable catalysts that could function in an acidic medium are highly desirable. In addition, the durability tests on the developed catalysts must be performed at high NH_3 yield rates to unveil their suitability for bulk NH_3 production. Apart from the H-type cell, the demonstration of NH_3 production from a prototype membrane electrode assembly (MEA) electrolyzer will pave the way for practical NH_3 synthesis. Besides, replacing of conventional anodic oxygen evolution reaction in the MEA electrolyzer with NO_x/SO_x oxidation reactions simultaneously produces the value-added NH_3 and nitric acid/sulfuric acid chemicals in the cathodic and anodic compartments, respectively.

In the future, screening of electrocatalysts to selectively produce urea from the co-reduction of NO and CO_2 will be of great significance. The sustainable urea generation using the MEA electrolyzer through the injection of the industrial exhaust (flue gas) could be a futuristic goal. With sincere efforts in electrocatalyst development and rigorous evaluation methods, we anticipate that the production of value-added products from pollutants could be realized soon.

Conflicts of interest

There are no conflicts to declare.

Acknowledgements

This research was supported by the Mid-level Research Program through the National Research Foundation of Korea (NRF) grant funded by the Ministry of Education (No. 2021R1A2C2009223).

References

1 L. A. White, *Am. Anthropol.*, 1943, **45**, 335–356.
2 R. Madlener and Y. Sunak, *Sustain. Cities Soc.*, 2011, **1**, 45–53.
3 S. Franco, V. R. Mandla and K. Ram Mohan Rao, *Renewable Sustainable Energy Rev.*, 2017, **71**, 898–907.
4 R. Avtar, S. Tripathi, A. K. Aggarwal and P. Kumar, *Resources*, 2019, **8**, 136.
5 U. Gierałtowska, R. Asyngier, J. Nakonieczny and R. Salahodjaev, *Energies*, 2022, **15**, 3390.
6 A. Javaid, N. Arshed, M. Munir, Z. A. Zakaria, F. S. Alamri, H. Abd El-Wahed Khalifa and U. Hanif, *Sustainability*, 2022, **14**, 669.
7 L. Chen, G. Msigwa, M. Yang, A. I. Osman, S. Fawzy, D. W. Rooney and P. S. Yap, *Environ. Chem. Lett.*, 2022, **20**, 2277–2310.
8 M. J. B. Kabeyi and O. A. Olanrewaju, *Front. Energy Res.*, 2022, **9**, 743114.
9 U.S. Energy Information Administration, Monthly Energy Review-03, 2021, **https://www.eia.gov/totalenergy/data/monthly/archive/00352103.pdf**.
10 R. Li, Y. Liu and Q. Wang, *Mar. Policy*, 2022, **143**, 105125.
11 O. B. Inal, B. Zincir and C. Deniz, *Int. J. Hydrog. Energy*, 2022, **47**, 19888–19900.
12 L. Chen, G. Msigwa, M. Yang, A. I. Osman, S. Fawzy, D. W. Rooney and P. S. Yap, *Environ. Chem. Lett.*, 2022, **20**, 2277–2310.
13 C. A. Horowitz, *Materials*, 2016, **55**, 740–755.
14 O. Nisiforou, L. M. Shakou, A. Magou and A. G. Charalambides, *Sustainability*, 2022, **14**, 2185.
15 W. S. Sou, T. Goh, X. N. Lee, S. H. Ng and K. H. Chai, *Energy Policy*, 2022, **170**, 113239.
16 M. Salimi, M. Hosseinpour and T. N. Borhani, *Energies*, 2022, **15**, 6064.
17 T. Capurso, M. Stefanizzi, M. Torresi and S. M. Camporeale, *Energy Convers. Manag.*, 2022, **251**, 114898.
18 S. Wu, N. Salmon, M. M. J. Li, R. Bañares-Alcántara and S. C. E. Tsang, *ACS Energy Lett.*, 2022, **7**, 1021–1033.
19 C. Sun, X. Fan, Y. Li, H. Han, J. Zhu, L. Liu and X. Geng, *Renew. Energ.*, 2022, **201**, 700–711.
20 S. J. Oh, J. H. Yoon, K. S. Jeon and J. J. Choi, *J. Mech. Sci. Technol.*, 2022, **36**, 1579–1586.

21 D. R. MacFarlane, P. V. Cherepanov, J. Choi, B. H. R. Suryanto, R. Y. Hodgetts, J. M. Bakker, F. M. Ferrero Vallana and A. N. Simonov, *Joule*, 2020, **4**, 1186–1205.
22 W. S. Chai, Y. Bao, P. Jin, G. Tang and L. Zhou, *Renewable Sustainable Energy Rev.*, 2021, **147**, 11254.
23 A. Valera-Medina, F. Amer-Hatem, A. K. Azad, I. C. Dedoussi, M. De Joannon, R. X. Fernandes, P. Glarborg, H. Hashemi, X. He, S. Mashruk, J. McGowan, C. Mounaim-Rouselle, A. Ortiz-Prado, A. Ortiz-Valera, I. Rossetti, B. Shu, M. Yehia, H. Xiao and M. Costa, *Energy Fuels*, 2021, **35**, 6964–7029.
24 O. B. Inal, B. Zincir and C. Deniz, *Int. J. Hydrog. Energy*, 2022, **47**, 19888–19900.
25 M. Wang, M. A. Khan, I. Mohsin, J. Wicks, A. H. Ip, K. Z. Sumon, C. T. Dinh, E. H. Sargent, I. D. Gates and M. G. Kibria, *Energy Environ. Sci.*, 2021, **14**, 2535–2548.
26 X. Liu, A. Elgowainy and M. Wang, *Green Chem.*, 2020, **22**, 5751–5761.
27 S. L. Foster, S. I. P. Bakovic, R. D. Duda, S. Maheshwari, R. D. Milton, S. D. Minteer, M. J. Janik, J. N. Renner and L. F. Greenlee, *Nat. Catal.*, 2018, **1**, 490–500.
28 Q. Liu, T. Xu, Y. Luo, Q. Kong, T. Li, S. Lu, A. A. Alshehri, K. A. Alzahrani and X. Sun, *Curr. Opin. Electrochem.*, 2021, **29**, 100766.
29 H.-J. Chen, Z.-Q. Xu, S. Sun, Y. Luo, Q. Liu, M. S. Hamdy, Z.-s Feng, X. Sun and Yan Wang, *Inorg. Chem. Front.*, 2022, **9**, 4608–4613.
30 D. K. Yesudoss, H. Chun, B. Han and S. Shanmugam, *Appl. Catal., B*, 2022, **304**, 120938.
31 B. H. R. Suryanto, K. Matuszek, J. Choi, R. Y. Hodgetts, H.-L. Du, J. M. Bakker, C. S. M. Kang, P. V. Cherepanov, A. N. Simonov and D. R. Macfarlane, *Science*, 2021, **372**, 1187–1191.
32 I. Zhu and T. Getting, *Environ. Technol. Rev.*, 2012, **1**, 46–58.
33 X. Zhang, Y. Wang, Y. Wang, Y. Guo, X. Xie, Y. Yu and B. Zhang, *Chem. Commun.*, 2022, **58**, 2777–2787.
34 J. Long, S. Chen, Y. Zhang, C. Guo, X. Fu, D. Deng and J. Xiao, *Angew. Chem., Int. Ed.*, 2020, **59**, 9711–9718.
35 B. H. R. Suryanto, H. L. Du, D. Wang, J. Chen, A. N. Simonov and D. R. MacFarlane, *Nat. Catal.*, 2019, **2**, 290–296.
36 Y.-I. Kwon, S. K. Kim, Y. B. Kim, S. J. Son, G. D. Nam, H. J. Park, W.-C. Cho, H. C. Yoon and J. H. Joo, *ACS Energy Lett.*, 2021, **6**, 4165–4172.
37 A. C. A. De Vooys, G. L. Beltramo, B. Van Riet, J. A. R. Van Veen and M. T. M. Koper, *Electrochim. Acta*, 2004, **49**, 1307–1314.
38 S.-C. Kuo, Z. Zhang, S. K. Ross, R. B. Klemm, R. D. Johnson, P. S. Monks, R. P. Thorn and L. J. Stief, *J. Phys. Chem. A*, 1997, **101**, 4035–4041.
39 M. W. Siegel, R. J. Celotta, J. L. Hall, J. Levine and R. A. Bennett, *Phys. Rev. A*, 1972, **6**, 607–631.
40 S. Sethuram Markandaraj, T. Muthusamy and S. Shanmugam, *Adv. Sci.*, 2022, **9**, 2201410.
41 T. Mou, J. Long, T. Frauenheim and J. Xiao, *ChemPlusChem*, 2021, **86**, 1211–1224.
42 M. Duca and M. T. M. Koper, *Energy Environ. Sci.*, 2012, **5**, 9726–9742.
43 H. Wan, A. Bagger and J. Rossmeisl, *Angew. Chem., Int. Ed.*, 2021, **60**, 21966–21972.
44 X. He, X. Li, X. Fan, J. Li, D. Zhao, L. Zhang, S. Sun, Y. Luo, D. Zheng, L. Xie, A. M. Asiri, Q. Liu and X. Sun, *ACS Appl. Nano Mater.*, 2022, **5**, 14246–14250.
45 J. Liang, Q. Liu, A. A. Alshehri and X. Sun, *Nano Res. Energy*, 2022, **1**, e9120010.
46 Q. Liu, L. Xie, J. Liang, Y. Ren, Y. Wang, L. Zhang, L. Yue, T. Li, Y. Luo, N. Li, B. Tang, Y. Liu, S. Gao, A. A. Alshehri, I. Shakir, P. O. Agboola, Q. Kong, Q. Wang, D. Ma and X. Sun, *Small*, 2022, **18**, 2106961.
47 X. Xu, L. Hu, Z. Li, L. Xie, S. Sun, L. Zhang, J. Li, Y. Luo, X. Yan, M. S. Hamdy, Q. Kong, X. Sun and Q. Liu, *Sustain. Energy Fuels*, 2022, **6**, 4130–4136.
48 H. Wang, F. Zhang, M. Jin, D. Zhao, X. Fan, Z. Li, Y. Luo, D. Zheng, T. Li, Y. Wang, B. Ying, S. Sun, Q. Liu, X. Liu and X. Sun, *Mater. Today Phys.*, 2023, **30**, 100944.
49 Z. Li, J. Liang, Q. Liu, L. Xie, L. Zhang, Y. Ren, L. Yue, N. Li, B. Tang, A. A. Alshehri, M. S. Hamdy, Y. Luo, Q. Kong and X. Sun, *Mater. Today Phys.*, 2022, **23**, 100619.
50 H. Wang, J. Huang, J. Cai, Y. Wei, A. Cao, B. Liu and S. Lu, *Small Methods*, 2023, 2300169.
51 J. Cai, J. Huang, A. Cao, Y. Wei, H. Wang, X. Li, Z. Jiang, G. I. N. Waterhouse, S. Lu and S.-Q. Zang, *Appl. Catal., B*, 2023, **328**, 122473.
52 H. Qian, S. Xu, J. Cao, F. Ren, W. Wei, J. Meng and L. Wu, *Nat. Sustain.*, 2021, **4**, 417–425.
53 L. Han, S. Cai, M. Gao, J. Y. Hasegawa, P. Wang, J. Zhang, L. Shi and D. Zhang, *Chem. Rev.*, 2019, **119**, 10916–10976.
54 L. Zhang, J. Liang, Y. Wang, T. Mou, Y. Lin, L. Yue, T. Li, Q. Liu, Y. Luo, N. Li, B. Tang, Y. Liu, S. Gao, A. A. Alshehri, X. Guo, D. Ma and X. Sun, *Angew. Chem., Int. Ed.*, 2021, **60**, 25263–25268.
55 J. S.-Hernández, C. R. S.-Ramirez, E. R.-Meneses, M. L.-Trujillo, J.-A. Wang, L. L.-Rojas and A. M.-Robledo, *Appl. Catal., B*, 2019, **259**, 118048.
56 J. Long, C. Guo, X. Fu, H. Jing, G. Qin, H. Li and J. Xiao, *J. Phys. Chem. Lett.*, 2021, **12**, 6988–6995.
57 B. H. Ko, B. Hasa, H. Shin, Y. Zhao and F. Jiao, *J. Am. Chem. Soc.*, 2022, **144**, 1258–1266.
58 A. C. A. De Vooys, M. T. M. Koper, R. A. Van Santen and J. A. R. Van Veen, *Electrochim. Acta*, 2001, **46**, 923–930.
59 V. Rosca and M. T. M. Koper, *J. Phys. Chem. B*, 2005, **109**, 16750–16759.
60 J. A. Colucci, M. J. Foral and S. H. Lancer, *Electrochim. Acta*, 1985, **30**, 521–528.
61 J. F. E. Gootzen, R. M. Van Hardeveld, W. Visscher, R. A. Van Santen and J. A. R. Van Veen, *Red. Trav. Chim. Pays-Bas*, 1996, **115**, 480–485.
62 A. Clayborne, H.-J. Chun, R. B. Rankin and J. Greeley, *Angew. Chem., Int. Ed.*, 2015, **54**, 8255–8258.
63 H.-J. Chun, V. Apaja, A. Clayborne, K. Honkala and J. Greeley, *ACS Catal.*, 2017, **7**, 3869–3882.
64 I. Katsounaros, M. C. Figueiredo, X. Chen, F. Calle-Vallejo and M. T. M. Koper, *ACS Catal.*, 2017, **7**, 4660–4667.
65 T. Mou, J. Long, T. Frauenheim and J. Xiao, *ChemPlusChem*, 2021, **86**, 1211–1224.

66 A. C. A. De Vooys, M. T. M. Koper, R. A. Van Santen and J. A. R. Van Veen, *J. Catal.*, 2001, **202**, 387–394.
67 Y. Zang, Q. Wu, S. Wang, B. Huang, Y. Dai and Y. Ma, *J. Phys. Chem. Lett.*, 2022, **13**, 527–535.
68 P. Lv, D. Wu, B. He, X. Li, R. Zhu, G. Tang, Z. Lu, D. Ma and Y. Jia, *J. Mater. Chem. A*, 2022, **10**, 9707–9716.
69 T. Mou, J. Liang, Z. Ma, L. Zhang, Y. Lin, T. Li, Q. Liu, Y. Luo, Y. Liu, S. Gao, H. Zhao, A. M. Asiri, D. Ma and X. Sun, *J. Mater. Chem. A*, 2021, **9**, 24268–24275.
70 X. Guo, H. Du, F. Qu and J. Li, *J. Mater. Chem. A*, 2019, **7**, 3531–3543.
71 Y. Li, C. Cheng, S. Han, Y. Huang, X. Du, B. Zhang and Y. Yu, *ACS Energy Lett.*, 2022, **7**, 1187–1194.
72 H. Zhang, Y. Li, C. Cheng, J. Zhou, P. Yin, H. Wu, Z. Liang, J. Zhang, Q. Yun, A. L. Wang, L. Zhu, B. Zhang, W. Cao, X. Meng, J. Xia, Y. Yu and Q. Lu, *Angew. Chem., Int. Ed.*, 2023, **62**, e202213351.
73 J. Shi, C. Wang, R. Yang, F. Chen, N. Meng, Y. Yu and B. Zhang, *Sci. China: Chem.*, 2021, **64**, 1493–1497.
74 D. Y. Kim, D. Shin, J. Heo, H. Lim, J. A. Lim, H. M. Jeong, B. S. Kim, I. Heo, I. Oh, B. Lee, M. Sharma, H. Lim, H. Kim and Y. Kwon, *ACS Energy Lett.*, 2020, **5**, 3647–3656.
75 J. Choi, J. Choi, H. L. Du, H. L. Du, C. K. Nguyen, C. K. Nguyen, B. H. R. Suryanto, A. N. Simonov, A. N. Simonov, D. R. MacFarlane and D. R. MacFarlane, *ACS Energy Lett.*, 2020, **5**, 2095–2097.
76 Y. Xiong, Y. Li, S. Wan, Y. Yu, S. Zhang and Q. Zhong, *J. Hazard. Mater.*, 2022, **430**, 128451.
77 K. Chen, G. Wang, Y. Guo, D. Ma and K. Chu, *Nano Res.*, 2023, DOI: **10.1007/s12274-023-5556-7**.
78 L. Chen, W. Sun, Z. Xu, M. Hao, B. Li, X. Liu, J. Ma, L. Wang, C. Li and W. Wang, *Ceram. Int.*, 2022, **48**, 21151–21161.
79 S. Cheon, W. J. Kim, D. Y. Kim, Y. Kwon and J. I. Han, *ACS Energy Lett.*, 2022, **7**, 958–965.
80 T. Muthusamy, S. Sethuram Markandaraj and S. Shanmugam, *J. Mater. Chem. A*, 2022, **10**, 6470–6474.
81 D. Wang, Z.-W. Chen, K. Gu, C. Chen, Y. Liu, X. Wei, C. V. Singh and S. Wang, *J. Am. Chem. Soc.*, 2023, **145**, 6899–6904.
82 P. M. Krzywda, A. Paradelo Rodríguez, N. E. Benes, B. T. Mei and G. Mul, *ChemElectroChem*, 2022, **9**, e202101273.
83 I. M. Wasser, S. De Vries, P. Moënne-Loccoz, I. Schröder and K. D. Karlin, *Chem. Rev.*, 2002, **102**, 1201–1234.
84 N. Lehnert, B. W. Musselman and L. C. Seefeldt, *Chem. Soc. Rev.*, 2021, **50**, 3640–3646.
85 D. Malko, A. Kucernak and T. Lopes, *J. Am. Chem. Soc.*, 2016, **138**, 16056–16068.
86 J. Liang, H. Chen, T. Mou, L. Zhang, Y. Lin, L. Yue, Y. Luo, Q. Liu, N. Li, A. A. Alshehri, I. Shakir, P. O. Agboola, Y. Wang, B. Tang, D. Ma and X. Sun, *J. Mater. Chem. A*, 2022, **10**, 6454–6462.
87 Z. Li, Z. Ma, J. Liang, Y. Ren, T. Li, S. Xu, Q. Liu, N. Li, B. Tang, Y. Liu, S. Gao, A. A. Alshehri, D. Ma, Y. Luo, Q. Wu and X. Sun, *Mater. Today Phys.*, 2022, **22**, 100586.
88 Z. Li, Q. Zhou, J. Liang, L. Zhang, X. Fan, D. Zhao, Z. Cai, J. Li, D. Zheng, X. He, Y. Luo, Y. Wang, B. Ying, H. Yan, S. Sun, J. Zhang, A. A. Alshehri, F. Gong, Y. Zheng and X. Sun, *Small*, 2023, **19**, 2300291.
89 A. Wu, J. Lv, X. Xuan, J. Zhang, A. Cao, M. Wang, X.-Y. Wu, Q. Liu, Y. Zhong, W. Sun, Q. Ye, Y. Peng, X. Lin, Z. Qi, S. Zhu, Q. Huang, X. Li, H. B. Wu and J. Yan, *Adv. Energy Mater.*, 2023, **13**, 2204231.
90 C. Bai, S. Fan, X. Li, Z. Niu, J. Wang, Z. Liu and D. Zhang, *Adv. Funct. Mater.*, 2022, **32**, 2205569.
91 T. Wei, H. Bao, X. Wang, S. Zhang, Q. Liu, J. Luo and X. Liu, *ChemCatChem*, 2023, **15**, e202201411.
92 L. Zhang, Q. Zhou, J. Liang, L. Yue, T. Li, Y. Luo, Q. Liu, N. Li, B. Tang, F. Gong, X. Guo and X. Sun, *Inorg. Chem.*, 2022, **61**, 8096–8102.
93 T. Mou, J. Liang, Z. Ma, L. Zhang, Y. Lin, T. Li, Q. Liu, Y. Luo, Y. Liu, S. Gao, H. Zhao, A. M. Asiri, D. Ma and X. Sun, *J. Mater. Chem. A*, 2021, **9**, 24268–24275.
94 J. Liang, W. F. Hu, B. Song, T. Mou, L. Zhang, Y. Luo, Q. Liu, A. A. Alshehri, M. S. Hamdy, L. M. Yang and X. Sun, *Inorg. Chem. Front.*, 2022, **9**, 1366–1372.
95 J. Liang, Q. Zhou, T. Mou, H. Chen, L. Yue, Y. Luo, Q. Liu, M. S. Hamdy, A. A. Alshehri, F. Gong and X. Sun, *Nano Res.*, 2022, **15**, 4008–4013.
96 K. Chen, P. Shen, N. Zhang, D. Ma and K. Chu, *Inorg. Chem.*, 2023, **62**, 653–658.
97 G. Meng, M. Jin, T. Wei, Q. Liu, S. Zhang, X. Peng, J. Luo and X. Liu, *Nano Res.*, 2022, **15**, 8890–8896.
98 P. Liu, J. Liang, J. Wang, L. Zhang, J. Li, L. Yue, Y. Ren, T. Li, Y. Luo, N. Li, B. Tang, Q. Liu, A. M. Asiri, Q. Kong and X. Sun, *Chem. Commun.*, 2021, **57**, 13562–13565.
99 G. Meng, T. Wei, W. Liu, W. Li, S. Zhang, W. Liu, Q. Liu, H. Bao, J. Luo and X. Liu, *Chem. Commun.*, 2022, **58**, 8097–8100.
100 K. Chen, Y. Tian, Y. Li, Y. Liu and K. Chu, *J. Mater. Chem. A*, 2023, **11**, 7409–7414.
101 D. Qi, F. Lv, T. Wei, M. Jin, G. Meng, S. Zhang, Q. Liu, W. Liu, D. Ma, M. S. Hamdy, J. Luo and X. Liu, *Nano Res. Energy*, 2022, **1**, e9120010.
102 J. Xi, H. S. Jung, Y. Xu, F. Xiao, J. W. Bae and S. Wang, *Adv. Funct. Mater.*, 2021, **31**, 2008318.
103 F. D. Speck, J. H. Kim, G. Bae, S. H. Joo, K. J. J. Mayrhofer, C. H. Choi and S. Cherevko, *JACS Au*, 2021, **1**, 1086–1100.
104 D. H. Kim, S. Ringe, H. Kim, S. Kim, B. Kim, G. Bae, H.-S. Oh, F. Jaouen, W. Kim, H. Kim and C. H. Choi, *Nat. Commun.*, 2021, **12**, 1856.
105 K. Chen, G. Zhang, X. Li, X. Zhao and K. Chu, *Nano Res.*, 2023, **16**, 5857–5863.
106 X. Peng, Y. Mi, H. Bao, Y. Liu, D. Qi, Y. Qiu, L. Zhuo, S. Zhao, J. Sun, X. Tang, J. Luo and X. Liu, *Nano Energy*, 2020, **78**, 105321.
107 X. Li, K. Chen, X. Lu, D. Ma and K. Chu, *Chem. Eng. J.*, 2023, **454**, 140333.
108 K. Chen, J. Wang, J. Kang, X. Lu, X. Zhao and K. Chu, *Appl. Catal., B*, 2023, **324**, 122241.
109 W. Zhang, X. Qin, T. Wei, Q. Liu, J. Luo and X. Liu, *J. Colloid Interface Sci.*, 2023, **638**, 650–657.
110 K. Chen, J. Wang, H. Zhang, D. Ma and K. Chu, *Nano Lett.*, 2023, **23**, 1735–1742.

111 Y. Lin, J. Liang, H. Li, L. Zhang, T. Mou, T. Li, L. Yue, Y. Ji, Q. Liu, Y. Luo, N. Li, B. Tang, Q. Wu, M. S. Hamdy, D. Ma and X. Sun, *Mater. Today Phys.*, 2022, **22**, 100611.
112 X. Li, G. Zhang, P. Shen, X. Zhao and K. Chu, *Inorg. Chem. Front.*, 2022, **10**, 280–287.
113 J. Liang, P. Liu, Q. Li, T. Li, L. Yue, Y. Luo, Q. Liu, N. Li, B. Tang, A. A. Alshehri, I. Shakir, P. O. Agboola, C. Sun and X. Sun, *Angew. Chem., Int. Ed.*, 2022, **61**, e202202087.
114 G. Zhang, Y. Wan, H. Zhao, Y. Guo and K. Chu, *Dalton Trans.*, 2023, **52**, 6248–6253.
115 K. Chen, Y. Zhang, J. Xiang, X. Zhao, X. Li and K. Chu, *ACS Energy Lett.*, 2023, **8**, 1281–1288.
116 K. Chen, Y. Zhang, W. Du, Y. Guo and K. Chu, *Inorg. Chem. Front.*, 2023, **10**, 2708–2715.
117 L. Ouyang, Q. Zhou, J. Liang, L. Zhang, L. Yue, Z. Li, J. Li, Y. Luo, Q. Liu, N. Li, B. Tang, A. Ali Alshehri, F. Gong and X. Sun, *J. Colloid Interface Sci.*, 2022, **616**, 261–267.
118 K. Li, Z. Shi, L. Wang, W. Wang, Y. Y. Liu, H. Cheng, Y. Yang and L. Zhang, *J. Hazard. Mater.*, 2023, **448**, 130890.
119 Q. Liu, Y. Lin, L. Yue, J. Liang, L. Zhang, T. Li, Y. Luo, M. Liu, J. You, A. A. Alshehri, Q. Kong and X. Sun, *Nano Res.*, 2022, **15**, 5032–5037.
120 K. Chen, N. Zhang, F. Wang, J. Kang and K. Chu, *J. Mater. Chem. A*, 2023, **11**, 6814–6819.